International Journal of Engineering Science 101 (2016) 126–155

Contents lists available at ScienceDirect

International Journal of Engineering Science

journal homepage: www.elsevier.com/locate/ijengsci

A numerical study of isotropic and anisotropic constitutive models with relevance to healthy and unhealthy cerebral arterial tissues

Paolo Tricerri[a,b,*], Luca Dedè[a], Alberto Gambaruto[c], Alfio Quarteroni[a,d], Adélia Sequeira[b]

[a] Chair of Modeling and Scientific Computing, E'cole Polytechnique Fe'de'rale de Lausanne, Av. Piccard, Station 8, 1015 Lausanne, Vaud, Switzerland

[b] Department of Mathematics & Center for Computational and Stochastic Mathematics, Instituto Superior Técnico, Universidade de Lisboa, Av. Rovisco Pais 1, 1049-001 Lisbon, Portugal

[c] M. Smoluchowski Institute of Physics and M.Kac Complex Systems Research Center, Jagiellonian University, Ul. Lojasiewicza 11, 30-348 Krakow, Poland

[d] MOX-Modeling and Scientific Computing, Dipartimento di Matematica "F. Brioschi", Politecnico di Milano, via Bonardi 9, 20133 Milano, Italy

ARTICLE INFO

Article history:
Received 22 July 2014
Revised 8 January 2016
Accepted 17 January 2016

Keywords:
Cerebral arterial tissue
Hyperelastic isotropic materials
Hyperelastic anisotropic materials
Multi-mechanism
Mechanical weakening
Finite elements

ABSTRACT

This paper presents an analysis of hyperelastic constitutive models for continuous bodies both from a modeling and numerical point of view. Contributions are made within the context of finite element numerical simulations. Numerical results with relevance to flows in the cardiovascular system are outlined in the case of a sophisticated fluid–structure interaction problem, in specific complex geometries of anatomically accurate cerebral arteries in diseased state. In this regard, the work carefully outlines the numerical validation of constitutive models for healthy and unhealthy cerebral arterial tissues by means of simulations of static inflation tests on an idealized specimen of anterior cerebral artery (ACA). The healthy tissue is described by means of isotropic and anisotropic models that, are fitted with respect to experimental data describing the mechanical behavior of the ACA; the numerical results are presented highlighting the most important numerical aspects influencing the correct and efficient simulation of the mechanics of continuous bodies such as, for instance, the arterial wall. We further consider numerical simulations of unhealthy conditions of the tissue by taking into account different levels of weakening of its mechanical properties. Taking the cerebral cardiovascular system as a challenging test problem, we focus on the study of the effects of the imposed mechanical levels of degradation on kinematic quantities of interest by simulating static inflation tests for the different models. This work does not aim to propose a new mathematical model for the mechanical damage occurring at the onset of cardiovascular diseases such as cerebral aneurysms. The modeling and numerical techniques presented may be applied to a wide range of problems,

* Corresponding author at: Chair of Modeling and Scientific Computing, E'cole Polytechnique Fe'de'rale de Lausanne, Av. Piccard, Station 8, Lausanne, Vaud 1015, Switzerland. Tel.: +44778477553.
E-mail address: paolotricerri@gmail.com (P. Tricerri).

http://dx.doi.org/10.1016/j.ijengsci.2016.01.002

equally challenging to that of the cardiovascular system with complex structural models and fluid–structure coupling.

1. Introduction

In continuum mechanics constitutive models aim at capturing the features of interest of the mechanical behavior of a continuous body under consideration, e.g. elasticity, nonlinearity or anisotropy (Truesdell & Noll, 1965). Bodies can be described at different modeling scales, e.g. microscopic or macroscopic. When a microscopic scale is adopted, the mechanical behavior of a body is described by considering the dynamics of each of its particles and their interactions; on the other hand, at the macroscopic scale, a body is modeled by means of certain field quantities. In this work, we present and discuss nonlinear macroscopic constitutive laws that have been proposed for the mathematical modeling of biological tissues, particularly the modeling of human arterial tissues. Some of the models, such as the neo-Hookean, Mooney–Rivlin, or anisotropic constitutive relations of the same form as the ones considered here, commonly used to describe biological tissues (e.g. Torii, Oshima, Kobayashi, Takagi, & Tezduyar, 2006; Chen, Wang, Ding, Yang, & Li, 2009; Valencia et al., 2013; Bazilevs et al., 2010; Isaksen et al., 2008), can be employed for the study of the mechanical behavior of other materials; for instance, elastomers (see e.g. Boyce & Arruda, 2000, and references therein) or rubber like materials, see Ciarletta, Izzo, Micera, and Tendick (2011). However, in this paper we confine ourselves to the context of biomechanics. For more general and advanced materials, we refer the reader e.g. to Criscione, Humphrey, Douglas, and Hunter (2000); Rajagopal (2003), and Criscione and Rajagopal (2013).

In the last decades we have witnessed an increased use of mathematical models and numerical simulations for the study of the cardiovascular system. This development has improved the ability to faithfully describe and simulate aspects of the complex physical processes involved, contributing to the progress in healthcare technologies. While investigation of cerebral aneurysms is considered in this work, the problem of choice may equally be generalized to other fluid–structure interaction problems. Extensive detail of the modeling challenges, the sophistication of the current state-of-the-art, details on methods for parameter setting and the validation of the models and simulations are presented in the context of biomedical simulations. Equally, the mathematical models and numerical methods outlined, are widely applicable to other problems of choice.

The present study provides an extensive numerical validation of existing constitutive models that have been used to describe human arteries. Based on this validation, we analyze and identify isotropic and anisotropic constitutive models that can be effectively employed in numerical simulations of the fluid–structure interaction problem concerning the hemodynamics in compliant arteries in the cerebral vasculature harboring aneurysms. To the best of our knowledge, this work represents the first extensive numerical validation of isotropic and anisotropic models for human cerebral arteries and establishes the basis for more complex studies, as already done for fluid–structure interaction simulations with both isotropic and anisotropic constitutive laws in Tricerri et al. (2015). A similar validation was considered in Hollander, Durban, Lu, Kassab, and Lanir (2011) for three isotropic and anisotropic models for porcine coronary arteries. In Polzer et al. (2013) numerical simulations for abdominal aortic aneurysmal tissues mechanics are proposed, but only for isotropic models under biaxial mechanical tests.

As other biological tissues, arteries feature a highly heterogeneous composition accounting for different types of connective and muscular tissues, cells and liquids. For this reason, constitutive models formulated within the framework of mixture theory have been proposed (see e.g. Truesdell & Noll, 1965; Humphrey & Rajagopal, 2002; Baek, Rajagopal, & Humphrey, 2006; Rajagopal & Tao, 1995). In spite of the mixture-composite nature of biological tissues, when characterizing their mechanical properties, it may be sufficient to consider models proposed within the theories of hyperelasticity or viscoelasticity. For instance, proximal arteries (i.e. arteries located close to the heart) of elastic type are commonly represented by means of hyperelastic models (Balzani, 2006), while distal arteries of muscular type can be described either as hyperelastic materials (Dalong & Robertson, 2009; Wulandana & Robertson, 2005) or by taking into account their viscoelastic and pseudoelastic response (Fung, Fronek, & Patitucci, 1979; Holzapfel & Gasser, 2001). The mechanical conditions of interest for which the hyperelastic, viscoelastic and pseudoelastic models have been proposed to characterize the mechanical behavior of the arterial tissue (see e.g. Holzapfel & Gasser, 2001; Fung et al., 1979; Dalong & Robertson, 2009) are represented by the physiological hemodynamical loads and vessel wall displacements occurring during one heart beat. In this work, only hyperelastic laws are considered to model the cerebral arterial tissue since in Kenneth, Barbaro, and Manley (2008); McGloughlin (2011); Monson (2001); Monson, Goldsmith, Barbaro, and Manley (2006); Scott, Ferguson, and Roach (1972), where experimental measurements of stress–strain relation for cerebral arteries are presented, viscoelastic effects on the mechanical response of the vessel wall are not reported. Arteries show both active and passive mechanical responses to external loads. Here, we focus on the mathematical models proposed for the latter which is determined by the mechanical properties of the elastin and collagen fibers (Holzapfel & Gasser, 2000; Humphrey, 2003). The typical passive mechanical behavior of healthy arteries is highly nonlinear and anisotropic with a stiffening effect occurring at high stresses

(Burton, 1954; Nichols & O'Rourke, 1998; Roach & Burton, 1957); such effect is due to the recruitment of the collagen fibers embedded in the elastin network of the media and adventitia layers.

This paper is concerned with the numerical validation of isotropic and anisotropic mathematical models for the description of the in vitro passive mechanical behavior of healthy cerebral arteries; in vivo effects as perivascular tissue and active contraction of the arterial tissue are not considered in this study. We remark that the choice of employing both isotropic and anisotropic models is driven by the fact that both classes of constitutive laws are largely used nowadays in the Computational Mechanics and Bioengineering communities; for this reason, we aim at addressing the numerical validation of mathematical models that represent the state of the art of arterial tissue modeling. As discussed in Humphrey (2003), several mathematical models have been proposed for biological tissues, in particular blood vessels (Fung, 1993; Humphrey, 2002). Among these, most of the constitutive laws describe the vessel wall, at the macroscopic scale, as a continuous body whose mechanical behavior is modeled according to the finite elasticity theory (Fung, 1993; Holzapfel, 2000; Holzapfel & Gasser, 2000; Humphrey, 2003). The most common constitutive laws are of phenomenological type, for which isotropic models represent the artery as a single layer material (Delfino, Stergiopulos, Moore, & Meister, 1997; Fung, 1993). Isotropic constitutive laws are largely used to model the arterial tissue due to their simplicity and the limited number of material parameters that usually need to be estimated to characterize the mechanical response. For instance, the Mooney–Rivlin and the neo-Hookean models have been largely used in literature to describe the arterial tissue within the context of fluid–structure interaction numerical simulations of the cerebral vasculature (Bazilevs et al., 2010; Chen et al., 2009; Isaksen et al., 2008; Torii et al., 2006; Valencia et al., 2013). However, they turned out to be inappropriate to fit the experimental data considered in this work (Scott et al., 1972). For that reason in this paper we use isotropic laws based on the St. Venant–Kirchhoff (Holzapfel, 2000) and exponential type models (Delfino et al., 1997).

Based on the experimental observations of the anisotropic mechanical response of the arterial tissue, several anisotropic models have been formulated to include in the constitutive laws the mechanical contribution of the collagen fibers. Such models rely on the mechanical theory of fiber-reinforced composites (Spencer, 1984). In this work, the tissue is assumed to be composed by a single layer embedding two constituents: the so called background material (whose main constituent is the elastin) and the fibrous network (i.e. the collagen fibers) which endows the tissue with its anisotropic response to external loads. Such choice is motivated by the fact that, although multi-layer constitutive models have been considered in literature for different types of arteries (e.g. Holzapfel & Gasser, 2000; Balzani, Neff, Schröder, & Holzapfel, 2006a; Dalong, Robertson, Lin, & Lovell, 2012), to the best of our knowledge, layer-specific experimental data for the elastic properties of cerebral arteries are not available in literature, as also pointed out in Dalong et al. (2012). The mechanical response of the background material is usually described by isotropic models, while the mechanical contribution of the collagen fibers is represented by a finite number of fiber families (Balzani, Brinkhues, & Holzapfel, 2012; Brands, Klawonn, Rheinbach, & Schröder, 2008; Calvo, Pẽna, Martinez, & Doblaré, 2007; Dalong & Robertson, 2009; Gasser & Holzapfel, 2006), each of them oriented along a characteristic direction for the tissue at rest. In this work, the recruitment of the collagen fibers is supposed to occur either at zero strains (Balzani et al., 2012; Gasser & Holzapfel, 2006), or at finite strains (Dalong & Robertson, 2009; Wulandana & Robertson, 2005), yielding the so called multi-mechanism constitutive law. We remark that the multi-mechanism model in Dalong and Robertson (2009); Wulandana and Robertson (2005) was specifically proposed after the analysis of the experimental measurements reported in Scott et al. (1972); for this reason we consider this set of data. However, other studies have focused either on the characterization of the mechanical behavior of cerebral arteries by considering inflation-extension tests (Monson, Barbaro, & Manley, 2008; Monson et al., 2006) or on the mechanical properties of other arteries (e.g. Sommer, Regitnig, Költringer, & Holzapfel, 2010; Kamenskiy et al., 2012).

The arterial tissue behaves as a nearly incompressible material within the physiological range of deformations (Carew, Vaishnav, & Patel, 1968). We enforce the nearly incompressibility constraint by penalizing the deformations of the tissue leading to changes in its volume for which we employ the approach based on the multiplicative decomposition of deformation tensor into a volumetric and an isochoric part (Flory, 1961; Odgen, 1997). The numerical validation of the constitutive models is carried out by means of finite elements simulations of static inflation tests on a computational domain representing a specimen of an anterior cerebral artery for which experimental measurements of the strain–stress relation are provided in Scott et al. (1972).

Afterward, we consider the mathematical modeling and numerical simulations of unhealthy cerebral arterial tissue. Cardiovascular diseases such as cerebral aneurysms are related to degenerative changes in the mechanical properties of the vessel wall driven by a complex interaction of biological and hemodynamic factors. In this work, the weakening of the arterial tissue that occurs in diseased states of arteries, as in the early stages formation of a cerebral aneurysm, is described by means of an isotropic weakening model for the background material (elastin). According to the approach proposed in Kachanov (1958), the level of mechanical weakening of the tissue is introduced in the constitutive model for healthy cerebral arterial tissue by means of a dimensionless parameter $D \in [0, 1)$. In literature (e.g. Dalong et al., 2012; Balzani et al., 2012; Calvo et al., 2007; Balzani, Schöder, & Gross, 2006b; Li & Robertson, 2009), different mathematical models have been proposed to describe the time evolution of the dimensionless parameter D as a function of both the mechanical and hemodynamical forces and stresses. Besides the difficulty of tuning the evolution of the parameter D with the progressive weakening of the arterial wall, in this work we are interested in studying the influence of the material model on the deformation and stresses distribution throughout the body during static inflation tests. For this reason, the different levels of mechanical weakening are imposed a priori, by means of preset values of the parameters D, suitably chosen to consistently compare the material models. We remark that this work does not aim at proposing a new mathematical model for the mechanical

damage occurring in the onset of a cerebral aneurysm; rather, we focus on the study of the effects of the imposed mechanical levels of degradation on kinematic quantities of interest by simulating static inflation tests for the different models, including the multi-mechanism law.

The paper is organized as follows. Section 2 introduces the kinematics quantities for the formulation of the constitutive laws and presents the mathematical models used to describe the healthy cerebral arterial tissue; in addition, the weakening model for the arterial tissue is presented. Section 3 deals with the finite element approximation of the linear momentum equation governing the deformations of the tissue under the action of external forces. The numerical results are presented and discussed in Section 4. In addition, in Section 4 we present and discuss results obtained from fluid–structure interaction simulations on a patient-specific geometry of a cerebral artery using some of the constitutive models previously discussed; in particular, our discussion of the numerical results focuses on mechanical indicators including the rupture risk. Conclusions follow in Section 5.

2. Mathematical modeling of the arterial tissue

This section deals with the mathematical modeling of the arterial tissue by taking into account the macroscopic nature of the vessel wall. Section 2.1 introduces the basic notations used to describe the motion of a continuous body under the action of external forces. Section 2.2 presents the mathematical models for the description of the healthy cerebral arterial tissue. Section 2.3 focuses on the description of the experimental data fitting procedure for estimating the material parameters of the constitutive laws. Section 2.4 deals with the mathematical modeling of unhealthy arterial tissue. In Section 2.5 we describe the choice of the weakening parameter D for the comparisons of different constitutive models representing unhealthy cerebral arterial tissues.

2.1. Kinematics of continuous media

The arterial tissue is assumed to be a continuous medium (also referred as continuous body) whose elastic properties are represented by suitable mathematical models. The kinematics of the vessel wall is described in terms of the vectorial and tensorial fields defined for the continuum theory (Holzapfel, 2000); the constitutive models (laws) are formulated under the finite elasticity assumption (Humphrey, 2003).

Let $\mathcal{B}_0 \subset \mathbb{R}^3$ and $\mathcal{B} \subset \mathbb{R}^3$ be the reference and current configuration of a continuous body, respectively. The position of a point in $\mathcal{B}_0$ is indicated by the material coordinates $\boldsymbol{X}$, while, in the current configuration, by the spatial coordinates $\boldsymbol{x}$. The motion from $\mathcal{B}_0$ to $\mathcal{B}$ experienced by the body under the action of external forces is described by the nonlinear function $\phi(\boldsymbol{X}, t)$that maps any point $\boldsymbol{X} \in \mathcal{B}_0$ into the point $\boldsymbol{x} \in \mathcal{B}$ at each time $t \in \mathbb{R}_+$. The material (i.e. Lagrangian) description of the displacement at each point $\boldsymbol{X} \in \mathcal{B}_0$ is represented by the vector $\boldsymbol{d}(\boldsymbol{X}) = \boldsymbol{x} - \boldsymbol{X} \in \mathbb{R}^3$. Locally, the deformations of the body in the material coordinates are described by the deformation gradient tensor $\boldsymbol{F}$, the local volume ratio J (also referred as Jacobian) and the right Cauchy–Green tensor $\boldsymbol{C}$ defined as:

$$\boldsymbol{F} = \nabla_{\boldsymbol{X}}\phi = \nabla_{\boldsymbol{X}}\boldsymbol{d} + \boldsymbol{I}, \quad J = \det(\boldsymbol{F}) > 0, \quad \text{and} \quad \boldsymbol{C} = \boldsymbol{F}^T\boldsymbol{F}, \tag{1}$$

respectively; $\nabla_{\boldsymbol{X}}\boldsymbol{d}$ is the material gradient of the displacement field and $\boldsymbol{I}$ is the second order identity tensor in $\mathbb{R}^3$ (Holzapfel, 2000). We focus on the mathematical modeling of the passive mechanical response of the arterial tissue which is assumed to be an hyperelastic material whose mechanical behavior is characterized by means of a scalar-valued function of the deformations (measured either by $\boldsymbol{F}$ or $\boldsymbol{C}$), the so called strain energy function $\mathcal{W}$ (Holzapfel, 2000). The stresses that occur in the body during its motion are measured in both the reference and current configuration through the first Piola–Kirchhoff tensor $\boldsymbol{P}$ and the Cauchy stress tensor $\boldsymbol{\sigma}$ defined, respectively, as:

$$\boldsymbol{P} = \frac{\partial \mathcal{W}}{\partial \boldsymbol{F}} \quad \text{and} \quad \boldsymbol{\sigma} = \frac{1}{J}\boldsymbol{P}\boldsymbol{F}^T. \tag{2}$$

The mechanical response of the body to external loads is governed by the linear momentum equation in Lagrangian form complemented by suitable boundary conditions. Since in this work we specifically consider inflation tests on cylindrical specimen of arteries, the mechanical problem is defined in the computational domain $\mathcal{B}_0$ of Fig. 1(a) that represents a cylindrical geometry of internal radius r_0 and thickness h (as in Fig. 1(b)). The problem reads:

$$\text{find} \quad \boldsymbol{d} : \mathcal{B}_0 \to \mathbb{R}^3 \quad : \quad \begin{cases} \text{Div}(\boldsymbol{P}(\boldsymbol{d})) = \boldsymbol{0} & \text{in } \mathcal{B}_0, \\ \boldsymbol{P}\boldsymbol{n} = -p_{out}\boldsymbol{n} & \text{on } \Gamma_{out}, \\ \boldsymbol{P}\boldsymbol{n} = -p_{in}\boldsymbol{n} & \text{on } \Gamma_{in}, \\ \boldsymbol{d} = \boldsymbol{0} & \text{on } \Gamma_D, \end{cases} \tag{3}$$

where Γ_D is the subset of $\partial\mathcal{B}_0$ where homogeneous Dirichlet boundary conditions are imposed; the subsets Γ_{out} and Γ_{in} indicate the external and internal surfaces of the body and $\boldsymbol{n}$ is the outward directed, unit vector normal to the corresponding surface. p_{out} and p_{in} represent the pressures acting on Γ_{out} and Γ_{in} defining the transmural pressure $\Delta P = p_{in} - p_{out}$. We assume, for simplicity, that $p_{out} = 0$, thus yielding $\Delta P = p_{in}$ (see Fig. 1(b)). The undeformed internal radius ($r_0 = 0.033$ cm) and the vessel wall thickness ($h = 0.010$ cm) of the tissue represented in Fig. 1(b) correspond to the physiological

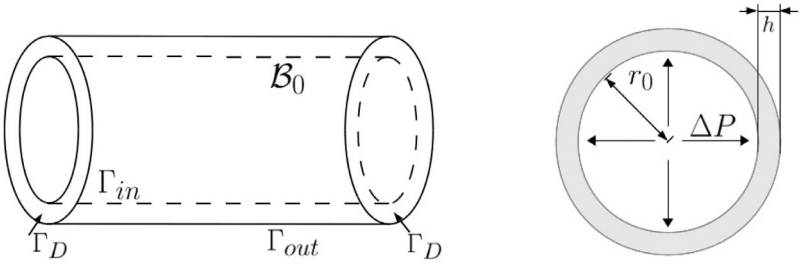

(a) Reference configuration $\mathcal{B}_0$

(b) Cross section of $\mathcal{B}_0$. $\Delta P = p_{in} - p_{out}$, $p_{out} = 0$.

Fig. 1. Computational domain $\mathcal{B}_0$ representing the arterial specimen and data of problem (3).

dimensions of the anterior cerebral artery described in Scott et al. (1972); Wulandana and Robertson (2005). We set the length L of the cylindrical specimen $L = 2$ cm. The range of transmural pressures considered to validate the different constitutive models is the physiological one occurring in cerebral arteries during one heart beat; therefore, $\Delta P \in [70, 150]$ mmHg (Dalong, 2009). We remark that the Dirichlet boundary conditions applied on Γ_D do not exactly represent the experimental setting described in Scott et al. (1972); indeed, in Scott et al. (1972) one of the two extremities of the specimen under consideration is ligated, while the other one is attached to the inflating apparatus. However, details about the axial deformations of the specimen during the inflation test are not provided in Scott et al. (1972) for which the unique component of the displacement that is presented is the one along the radial direction. For this reason, we have applied homogeneous Dirichlet conditions on both extremities and, in order to remove the boundary effects on the vessel wall displacement in the central portion of the cylindrical geometry, we have considered a computational domain of length $L = 30D$.

The arterial tissue behaves as a nearly incompressible material within the physiological range of deformations (Carew et al., 1968). In order to model such behavior, we adopt the approach based on the volumetric-isochoric split of the deformation gradient tensor $\boldsymbol{F}$ (Flory, 1961; Odgen, 1997) which has been used in literature (e.g. Bazilevs et al., 2010; Calvo et al., 2007; Gasser, Schulze-Bauer, & Holzapfel, 2002; Nobile, Pozzoli, & Vergara, 2013) for numerical simulations of the arterial tissue. According to Flory (1961), the local deformation gradient $\boldsymbol{F}$ and the right Cauchy–Green $\boldsymbol{C}$ tensors are split into a so called volumetric and an isochoric part by means of the relations:

$$\boldsymbol{F} = \left(J^{1/3}\boldsymbol{I}\right)\overline{\boldsymbol{F}} \quad \text{and} \quad \boldsymbol{C} = \left(J^{2/3}\boldsymbol{I}\right)\overline{\boldsymbol{C}}, \tag{4}$$

where the tensors $J^{1/3}\boldsymbol{I}$ and $J^{2/3}\boldsymbol{I}$ are associated with isotropic volume-changing deformations, while the tensors $\overline{\boldsymbol{F}} := J^{-1/3}\boldsymbol{F}$ and $\overline{\boldsymbol{C}} := J^{-2/3}\boldsymbol{C}$ with volume-preserving deformations of the material, for which $\det(\overline{\boldsymbol{F}}) \equiv \det(\overline{\boldsymbol{C}}) \equiv 1$. Based on this kinematic assumption, the strain energy function $\mathcal{W}$ can be reformulated in its penalty form as:

$$\mathcal{W} = \mathcal{W}(\boldsymbol{C}, J) = \mathcal{U}(J) + \overline{\mathcal{W}}(\overline{\boldsymbol{C}}), \tag{5}$$

where the volumetric term $\mathcal{U}(J)$ penalizes the volume-changing deformations and the isochoric part $\overline{\mathcal{W}}(\overline{\boldsymbol{C}})$ characterizes the mechanical response of the material to external loads according to different constitutive laws. The first Piola–Kirchhoff tensor $\boldsymbol{P}$ is defined according to Eq. (2) as:

$$\boldsymbol{P} = \widetilde{\boldsymbol{P}} + \overline{\boldsymbol{P}} = \frac{\partial \mathcal{U}(J)}{\partial \boldsymbol{F}} + \frac{\partial \overline{\mathcal{W}}(\overline{\boldsymbol{C}})}{\partial \boldsymbol{F}}, \tag{6}$$

where $\widetilde{\boldsymbol{P}}$ and $\overline{\boldsymbol{P}}$ measure the stresses due to volume-changing and isochoric deformations, respectively. We remark that, in order to guarantee the existence of realistic physical solutions of Eq. (3), the strain energy function in Eq. (5) has to satisfy the polyconvexity condition (see Ball, 1977; Balzani, 2006). In addition, both the functions $\mathcal{U}(J)$and $\overline{\mathcal{W}}(\overline{\boldsymbol{C}})$must satisfy the requirement of objectivity under changes of coordinates systems (Holzapfel, 2000). We discuss the choice of $\mathcal{U}$ and $\overline{\mathcal{W}}$ in Sections 2.2.1 and 2.2.2.

2.2. Volumetric and isochoric strain energy functions for the arterial tissue

2.2.1. The choice of the volumetric strain energy function $\mathcal{U}$

Due to the polyconvexity requirements on the strain energy function $\mathcal{W}$, the volumetric term $\mathcal{U} = \mathcal{U}(J)$ must be a strictly convex function of J endowed with a unique minimum in $J = 1$ (Holzapfel, 2000). This component of the strain energy function $\mathcal{W}$ can be chosen independently from the isochoric term $\overline{\mathcal{W}}$ of Eq. (5), even if the decomposition approach is effective only when the functions $\mathcal{U}$ and $\overline{\mathcal{W}}$ are properly balanced.

Different functions $\mathcal{U}$ have been proposed in literature (see for instance Miehe, 1994; Odgen, 1997; Simo & Taylor, 1991); in this work, it is assumed in the form:

$$\mathcal{U}(J) = \frac{\kappa}{4}\left[(J-1)^2 + \log^2 J\right], \tag{7}$$

in order to penalize the cases $J \neq 1$ and $J \to 0$ corresponding to unphysical solutions. The parameter κ, which can be interpreted as a bulk modulus, assumes the role of a user-specified penalty parameter that is suitably determined to weakly enforce the nearly incompressible response of the material in the physiological range of deformations of the body. The choice of the parameter κ is a trade-off between the need to represent the quasi-incompressible behavior of the tissue and to yield a physical meaningful displacement of the body.

2.2.2. The choice of the isochoric strain energy function $\overline{\mathcal{W}}$

We consider the healthy arterial tissue as a homogeneous body with constant material parameters for which the layered structure of the vessel wall is neglected. As described in Nichols and O'Rourke (1998), the arteries show a highly non-linear and anisotropic mechanical behavior. In the last decades, structurally motivated models (as for instance anisotropic laws), that take into account the fibrous nature of the tissue into the constitutive relation, have been proposed and used to represent the anisotropic behavior of arteries (Dalong & Robertson, 2009; Holzapfel & Gasser, 2000; Kroon & Holzapfel, 2008). However, isotropic models are still largely used to represent the arterial tissue (Fung, 1993; Holzapfel & Gasser, 2000; Humphrey, 2003). For this reason, we will consider both isotropic and anisotropic models. We remark that, in order for the strain energy function $\mathcal{W}$ to satisfy the polyconvexity condition for all the deformations of the body, also the isochoric strain energy function $\overline{\mathcal{W}}$ must be a polyconvex function for all states of deformations.

2.2.3. Constitutive models for isotropic bodies

When the arterial tissue is modeled by means of isotropic models, it is assumed to be composed by a unique elastic material by neglecting its fibrous nature. Due to requirements of frame indifference of the constitutive law (Holzapfel, 2000), the isochoric part of the strain energy function in Eq. (5), indicated as $\overline{\mathcal{W}}_{iso}$, is formulated in terms of the principal invariants of $\overline{\boldsymbol{C}}$, as:

$$\overline{\mathcal{W}}_{iso} = \overline{\mathcal{W}}_{iso}(\overline{\boldsymbol{C}}) = \overline{\mathcal{W}}_{iso}(\bar{I}_1, \bar{I}_2, \bar{I}_3) = \overline{\mathcal{W}}_{iso}(\bar{I}_1, \bar{I}_2), \tag{8}$$

where:

$$\bar{I}_1 = Tr(\overline{\boldsymbol{C}}) = J^{-2/3} I_1, \quad \bar{I}_2 = \frac{1}{2}\left[Tr^2(\overline{\boldsymbol{C}}) - Tr(\overline{\boldsymbol{C}}^2)\right] = J^{-4/3} I_2 \quad \text{, and } \bar{I}_3 = \det(\overline{\boldsymbol{C}}) = J^{-2} I_3, \tag{9}$$

with (I_1, I_2, I_3) the principal invariants of $\boldsymbol{C}$ (Holzapfel, 2000). We remark that the explicit dependency of $\overline{\mathcal{W}}_{iso}$ on $\bar{I}_3$ in Eq. (8) can be dropped since $\bar{I}_3 \equiv 1$, due to the definition of the isochoric right Cauchy–Green tensor $\overline{\boldsymbol{C}}$.

A common constitutive model is the St. Venant–Kirchhoff (SVK) (Holzapfel, 2000), for which:

$$\overline{\mathcal{W}}_{iso} = \overline{\mathcal{W}}_{iso}^{SVK}(\bar{I}_1, \bar{I}_2) = \left(\frac{\lambda}{8} + \frac{\mu}{4}\right)\bar{I}_1^2 - \left(\frac{3}{4}\lambda + \frac{\mu}{2}\right)\bar{I}_1 - \frac{\mu}{2}\bar{I}_2 + \frac{9}{8}\lambda + \frac{3}{4}\mu, \tag{10}$$

where λ and μ are the Lamé parameters, depending on the Young modulus E and Poisson's ratio ν as:

$$\lambda = \frac{E\nu}{(1+\nu)(1-2\nu)} \quad \text{and} \quad \mu = \frac{E}{2(1+\nu)}. \tag{11}$$

We recall that the Young modulus measures the mechanical stiffness of the material and the Poisson's ratio $\nu \in (0, 0.5)$ represents the relative change of volume of an elementary cube inside the body due to deformations of the material. We remark that the St. Venant–Kirchhoff law, and eventually its linearized approximation, is still largely used in the fluid–structure interaction numerical simulations of the blood flow in complaint arteries both in the case of cerebral arteries (Torii et al., 2006; 2008; Valencia et al., 2013) and other types of arteries (Crosetto, 2011; Malossi, 2012); for this reason, we will include the SVK model for a numerical comparison.

In addition, we consider the first order exponential (EXP1) model proposed in Delfino et al. (1997), for which:

$$\overline{\mathcal{W}}_{iso} = \overline{\mathcal{W}}_{iso}^{EXP1}(\bar{I}_1) = \frac{\alpha_1}{2\gamma_1}\left(e^{\gamma_1(\bar{I}_1 - 3)} - 1\right) \tag{12}$$

and the second order exponential model (EXP2) (Balzani, 2006):

$$\overline{\mathcal{W}}_{iso} = \overline{\mathcal{W}}_{iso}^{EXP2}(\bar{I}_1) = \frac{\alpha_2}{2\gamma_2}\left(e^{\gamma_2(\bar{I}_1 - 3)^2} - 1\right), \tag{13}$$

where α_1, α_2, γ_1 and γ_2 are suitable material parameters. In Eqs. (12) and (13) α_1 and α_2 measure the mechanical stiffness of the arterial tissue, while γ_1 and γ_2 are representative of the level of nonlinearity of the mechanical response of the vessel wall.

We remark that the strain energy functions associated to the exponential (EXP1 and EXP2) models of Eqs. (12) and (13) satisfy the polyconvexity condition for all the states of deformations (Balzani, 2006). Conversely, the SVK model does not satisfy this condition under compression states of deformations (Holzapfel, 2000; Raoult, 1986); however, we observe that this situation does not occur during inflation tests of cylindrical geometries like the one represented in Fig. 1(a).

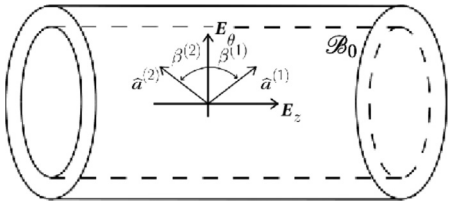

Fig. 2. Directions $\boldsymbol{a}_0^{(i)}$, $i = 1, 2,$ of the families of collagen fibers in the reference configuration $\mathcal{B}_0$.

2.2.4. Constitutive model for anisotropic bodies

When modeling the passive mechanical response of the vessel wall by means of anisotropic models, the tissue is assumed to be composed of an isotropic medium, also called background material, in which a network of collagen fibers is immersed (Holzapfel & Gasser, 2000; Humphrey, 2003). Such models describe the overall mechanical behavior of the arterial tissue as the sum of the contributions provided by its two main constituents. Based on experimental observations, the two constituents are the elastin and the collagen fibers respectively, that are the main components of the vessel wall (Holzapfel & Gasser, 2000; Nichols & O'Rourke, 1998). In literature (see Dalong, 2009; Balzani, 2006, and references therein) the anisotropic models commonly employed are based on the theory of fiber-reinforced composites (Spencer, 1984). The contribution of the collagen fibers to the overall mechanical behavior of the tissue is usually modeled as the sum of the mechanical responses of a finite number of families of collagen fibers. As described in Dalong and Robertson (2009); Wulandana and Robertson (2005), the collagen fibers contribute to the mechanical response of the arterial tissue only when activated. Indeed, the recruitment of the collagen fibers has been hypothesized as the underlying mechanism for the mechanical stiffening with increasing stress in arteries.

When the collagen fibers are activated, the isochoric strain energy function $\overline{\mathcal{W}}$characterizing anisotropic materials, that we indicate by $\overline{\mathcal{W}}_{aniso}$, is decomposed into the sum of the load-bearing contributions provided by the background material and the collagenous constituent as:

$$\overline{\mathcal{W}}_{aniso} = \overline{\mathcal{W}}_{aniso}^{bg} + \overline{\mathcal{W}}_{aniso}^{fibers}, \tag{14}$$

where $\overline{\mathcal{W}}_{aniso}^{bg}$ characterizes the background material and $\overline{\mathcal{W}}_{aniso}^{fibers}$ models the fiber-reinforcing component of the tissue. As described in Holzapfel and Gasser (2000), isotropic laws as those presented in Section 2.2.3 (SVK, EXP1, EXP2) can be used to describe the background material. Conversely, the component $\overline{\mathcal{W}}_{aniso}^{fibers}$ of $\overline{\mathcal{W}}_{aniso}$ takes into account for the anisotropic effects in the mechanical response of N families of collagen fibers. For any point $\boldsymbol{X}$ in the reference configuration $\mathcal{B}_0$, each family of collagen fibers is endowed with a characteristic direction $\boldsymbol{a}_0^{(i)}$, for $i = 1 \dots N$, as highlighted in Fig. 2. Due to the weak interactions between the fiber families (Holzapfel & Gasser, 2000), the strain energy function $\overline{\mathcal{W}}_{aniso}^{fibers}$ is written as the sum of N strain energy functions, $\overline{\mathcal{W}}_{aniso}^{fibers,(i)}$, each of them characterizing the mechanical behavior of the ith family, as:

$$\overline{\mathcal{W}}_{aniso}^{fibers} = \sum_{i=1}^{N} \overline{\mathcal{W}}_{aniso}^{fibers,(i)}. \tag{15}$$

The function $\overline{\mathcal{W}}_{aniso}^{fibers,(i)}$, due to frame indifference requirements, can be formulated in terms of the so called modified pseudo-invariants of $\overline{\boldsymbol{C}}$ and the second order tensor $(\boldsymbol{a}_0^{(i)} \otimes \boldsymbol{a}_0^{(i)})$ associated to the ith family (Holzapfel, 2000; Spencer, 1971), indicated by $\bar{I}_4^{(i)}$ and $\bar{I}_5^{(i)}$, as:

$$\overline{\mathcal{W}}_{aniso}^{fibers,(i)} = \overline{\mathcal{W}}_{aniso}^{fibers,(i)}\left(\bar{I}_4^{(i)}, \bar{I}_5^{(i)}\right), \tag{16}$$

where

$$\bar{I}_4^{(i)} = Tr\left(\overline{\boldsymbol{C}}\left(\boldsymbol{a}_0^{(i)} \otimes \boldsymbol{a}_0^{(i)}\right)\right) = J^{-2/3} Tr\left(\boldsymbol{C}\left(\boldsymbol{a}_0^{(i)} \otimes \boldsymbol{a}_0^{(i)}\right)\right) = J^{-2/3} I_4^{(i)}, \tag{17}$$

and

$$\bar{I}_5^{(i)} = Tr\left(\overline{\boldsymbol{C}}^2\left(\boldsymbol{a}_0^{(i)} \otimes \boldsymbol{a}_0^{(i)}\right)\right) = J^{-4/3} Tr\left(\boldsymbol{C}^2\left(\boldsymbol{a}_0^{(i)} \otimes \boldsymbol{a}_0^{(i)}\right)\right) = J^{-4/3} I_5^{(i)}, \tag{18}$$

being $I_4^{(i)}$ and $I_5^{(i)}$ the fourth and fifth invariants associated to $\boldsymbol{C}$ and the tensor $(\boldsymbol{a}_0^{(i)} \otimes \boldsymbol{a}_0^{(i)})$. From the mechanical point of view, $I_4^{(i)}$ corresponds to the square of the stretch of the body along the fiber direction $\boldsymbol{a}_0^{(i)}$, or alternatively, it can be interpreted as the square of the length of the deformed fiber in the current configuration; $I_5^{(i)}$ measures the deformations of the ith collagen fiber under shear conditions (Raoult, 2009). In the anisotropic models under consideration, we set either $\overline{\mathcal{W}}_{aniso}^{bg} = \overline{\mathcal{W}}_{iso}^{EXP1}$ or $\overline{\mathcal{W}}_{aniso}^{bg} = \overline{\mathcal{W}}_{iso}^{EXP2}$. The isochoric strain energy function for the single collagen fiber family $\overline{\mathcal{W}}_{aniso}^{fibers,(i)}$ in Eq. (15) is chosen as a second order exponential law along the fiber direction, that is:

$$\overline{\mathcal{W}}_{aniso}^{fibers,(i)}\left(\bar{I}_4^{(i)}, \bar{I}_5^{(i)}\right) = \overline{\mathcal{W}}_{aniso}^{fibers,(i)}\left(\bar{I}_4^{(i)}\right) = \frac{\alpha^{(i)}}{2\gamma^{(i)}}\left(e^{\gamma^{(i)}(\bar{I}_4^{(i)} - \|\boldsymbol{a}_A^{(i)}\|^2)^2} - 1\right), \tag{19}$$

where $\alpha^{(i)}$ and $\gamma^{(i)}$ are the mechanical stiffness and level of nonlinearity characterizing the ith family of collagen fibers, respectively, and $\|\boldsymbol{a}_A^{(i)}\|$ is called the activation length of the ith family of collagen fibers. From the modeling point of view, $\|\boldsymbol{a}_A^{(i)}\|$ is the length at which the recruitment of the ith family of collagen fibers occurs. The ith family of collagen fibers is considered activated, i.e. it contributes to the mechanical response of the arterial tissue, when $\bar{I}_4^{(i)}$ is higher than the square of the activation length $\|\boldsymbol{a}_A^{(i)}\|$ (Balzani, 2006; Dalong & Robertson, 2009). According to Balzani (2006); Gasser and Holzapfel (2006), the activation length corresponds to the length of the collagen fibers in the reference configuration $\mathcal{B}_0$; therefore, for this class of models, the ith family of collagen fibers is activated whenever the activation condition, $\bar{I}_4^{(i)} > \|\boldsymbol{a}_0^{(i)}\|^2$, is satisfied. In literature (see Balzani, 2006; Brinkhues, Klawonn, Rheinbach, & Schröder, 2013; Calvo et al., 2007; Gasser & Holzapfel, 2006), the length of the ith fiber family in the reference configuration $\mathcal{B}_0$ is usually set to 1. In the following, this constitutive model will be indicated as EXP2-RC. On the other hand, according to the multi-mechanism model (Dalong & Robertson, 2009; Wulandana & Robertson, 2005), the recruitment of the ith family of collagen fibers occurs whenever $\bar{I}_4^{(i)} > \|\boldsymbol{a}_{MM}^{(i)}\|^2$, where $\|\boldsymbol{a}_{MM}^{(i)}\|$ is the activation length associated to the ith family in a deformed configuration of the body $\mathcal{B}_{MM}^{(i)}$, called the activation configuration. In Dalong (2009), the activation length satisfies the condition $\|\boldsymbol{a}_{MM}^{(i)}\| > 1$ since, in the reference configuration $\mathcal{B}_0$, the collagen fibers are assumed of unitary length. The strain energy function for the collagen fibers in the multi-mechanism model will be indicated as EXP2-MM. We remark that the strain energy function $\overline{\mathcal{W}}_{aniso}^{fibers,(i)}$ in Eq. (19) satisfies the polyconvexity condition for all states of deformations (Balzani, 2006).

The full isochoric strain energy function $\overline{\mathcal{W}}_{aniso}$ in Eq. (14) for anisotropic material reads as follows:

$$\overline{\mathcal{W}}_{aniso}(\bar{I}_1, \bar{I}_2, \bar{I}_3, \bar{\mathbf{I}}_4, \bar{\mathbf{I}}_5) = \overline{\mathcal{W}}_{aniso}^{bg}(\bar{I}_1, \bar{I}_2) + \overline{\mathcal{W}}_{aniso}^{fibers}(\bar{\mathbf{I}}_4, \bar{\mathbf{I}}_5), \tag{20}$$

where $\bar{\mathbf{I}}_4 = \{\bar{I}_4^{(i)}\}_{i=1}^N$ and $\bar{\mathbf{I}}_5 = \{\bar{I}_5^{(i)}\}_{i=1}^N$ are the set of pseudo-invariants of the different fiber families. We remark that, similarly to Eq. (8), the dependency of $\overline{\mathcal{W}}_{aniso}$ on $\bar{I}_3$ has been dropped since $\bar{I}_3 \equiv 1$. When including the activation condition in Eq. (20), the general formulation of the isochoric strain energy function $\overline{\mathcal{W}}_{aniso}$ reads:

$$\overline{\mathcal{W}}_{aniso} = \begin{cases} \overline{\mathcal{W}}_{aniso}^{bg}(\bar{I}_1, \bar{I}_2), & \text{if} \quad \bar{\mathbf{I}}_4 \leq \|\boldsymbol{a}_A\|^2, \\ \overline{\mathcal{W}}_{aniso}^{bg}(\bar{I}_1, \bar{I}_2) + \overline{\mathcal{W}}_{aniso}^{fibers}(\bar{\mathbf{I}}_4, \bar{\mathbf{I}}_5), & \text{if} \quad \bar{\mathbf{I}}_4 > \|\boldsymbol{a}_A\|^2, \end{cases} \tag{21}$$

where $\|\boldsymbol{a}_A\|^2$ indicated the set of activation lengths $\{\|\boldsymbol{a}_A^{(i)}\|^2\}_{i=1}^N$. In Eq. (21), when assuming the activation length equal to the one in the reference configuration, $\|\boldsymbol{a}_A^{(i)}\|^2 = \|\boldsymbol{a}_0^{(i)}\|^2 = 1$, otherwise, for the multi-mechanism model, we have $\|\boldsymbol{a}_A^{(i)}\|^2 = \|\boldsymbol{a}_{MM}^{(i)}\|^2$. In Eq. (21), the condition $\bar{\mathbf{I}}_4 > \|\boldsymbol{a}_A\|^2$ is verified if there exists at least a fiber family i, with $i = 1, \ldots, N$, such that $\bar{I}_4^{(i)} > \|\boldsymbol{a}_A^{(i)}\|^2$. It is worth pointing out that, when the collagen fibers contribute to the mechanical response of the tissue, the isochoric part of the first Piola–Kirchhoff tensor $\bar{\boldsymbol{P}}$ for anisotropic models in Eq. (6) reads as follows:

$$\bar{\boldsymbol{P}}_{aniso} = \bar{\boldsymbol{P}}_{aniso}^{bg} + \bar{\boldsymbol{P}}_{aniso}^{fibers} = \bar{\boldsymbol{P}}_{aniso}^{bg} + \sum_{i=1}^{N} \bar{\boldsymbol{P}}_{aniso}^{fibers,(i)}. \tag{22}$$

We include the collagen recruitment in the definition of $\bar{\boldsymbol{P}}_{aniso}$ by means of an activation function that multiplies the contribution $\bar{\boldsymbol{P}}_{aniso}^{fibers,(i)}$ as follows:

$$\bar{\boldsymbol{P}}_{aniso} = \bar{\boldsymbol{P}}_{aniso}^{bg} + \sum_{i=1}^{N} \left(\frac{1}{\pi} \arctan(\epsilon(\bar{I}_4^{(i)} - \|\boldsymbol{a}_A^{(i)}\|^2)) + \frac{1}{2} \right) \bar{\boldsymbol{P}}_{aniso}^{fibers,(i)}, \tag{23}$$

where ϵ is a dimensionless user-specified parameter which we choose as $\epsilon = 5.0 \times 10^5$ to model the abrupt recruitment of the collagen fibers. We remark that, for small values of ϵ in Eq. (23) the recruitment of the collagen fibers becomes more gradual and the collagen fibers are described as mechanically active also for values of the stretch smaller than the activation stretch (Tricerri, 2014).

2.3. Determination of the material parameters from experimental data

In order to characterize the mechanical behavior of the healthy arterial tissue, it is necessary to estimate the material parameters of the isochoric constitutive models described in Section 2.2.2. Although in vitro mechanical inflation-extension and twist tests would be required to fully characterize the mechanical behavior of anisotropic materials (Holzapfel & Gasser, 2000; Holzapfel & Ogden, 2008), for the anisotropic constitutive models described in Section 2.2.4 biaxial data can be employed under the incompressibility assumption to completely describe the mechanical response of the healthy arterial tissue. In addition, we remark that for cerebral arteries, although some publications, as (Bell, Kunjir, & Monson, 2013; Kenneth et al., 2008; Monson et al., 2008), report biaxial measurements of the stress–strain relation to the best of our knowledge, the only full set of experimental measurements that can be employed in a data fitting procedure available in literature is reported in Scott et al. (1972). Therefore, in this work, the material parameters of each

Table 1
Material parameters and R^2 values for the isotropic models. E, α_1, α_2 [dyn/cm^2]; ν, γ_1, γ_2 [−].

Model ($\mathcal{W}_{iso}$)	Parameters	R^2
$\mathcal{W}_{iso}^{SVK}$	$E = 1.1420\times10^5$, $\nu = 0.4500$	0.9338
$\mathcal{W}_{iso}^{EXP1}$	$\alpha_1 = 7.6350\times10^4$, $\gamma_1 = 0.7410$	0.9942
$\mathcal{W}_{iso}^{EXP2}$	$\alpha_2 = 6.8220\times10^4$, $\gamma_2 = 0.0609$	0.9971

isochoric model are determined by computing the least-squares approximation (Quarteroni, Sacco, & Saleri, 2007) of experimental measurements of the strain–stress relation of cerebral arteries reported in Scott et al. (1972). In Scott et al. (1972) quasi-static inflation tests up to the transmural pressure (ΔP) of 200 mmHg on cylindrical specimens of healthy human anterior cerebral artery (ACA) are shown. We remark that this work focuses on an unidirectional analysis of the mechanical behavior of cerebral arteries. Indeed, in Scott et al. (1972) only the strain–stress relation along the circumferential direction is analyzed. However, as previously mentioned, we deal with an extensive numerical validation of existing constitutive models for human arteries in order to provide a contribution within the context of finite element realistic numerical simulations of cerebral arteries and the cardiovascular system at large. In this work, similarly to Dalong and Robertson (2009); Wulandana and Robertson (2005), the ACA is modeled as a cylindrical membrane of undeformed internal radius (r_0) and thickness (h) composed of a homogeneous and incompressible material. We remark that, in virtue of the incompressibility assumption (i.e. $J = 1$), the volumetric function $\mathcal{U}$ in Eq. (5) is identically null, while the modified invariants of $\overline{\boldsymbol{C}}$ coincide with the principal invariants of $\boldsymbol{C}$, being $\overline{\boldsymbol{C}} \equiv \boldsymbol{C}$ (see Eqs. (9), (17), and (18)). In Scott et al. (1972) the deformation of the internal radius is measured by the circumferential stretch, indicated by λ_r, that is defined as $\lambda_r = r/r_0$, with r being the deformed radius at a certain level of transmural pressure ΔP. In order to fit the experimental data we consider nonlinear functions $\mathcal{T} = \mathcal{T}(\lambda_r)$ (detailed in Sections 2.3.1 and 2.3.2) that relate the membrane tension $\mathcal{T}$ to the circumferential stretch λ_r as in Dalong and Robertson (2009); Naghdi (1984); Naghdi and Tang (1977); Wulandana and Robertson (2005). In addition, the membrane tension is related to the transmural pressure by means of the Young–Laplace equation, $\mathcal{T} = r\ \Delta P$ (Scott et al., 1972). For a given constitutive model for the cerebral arterial tissue, the nonlinear approximation of the experimental data is computed by means of the Levenberg–Marquardt least-squares method (Marquardt, 1963).

Once the material parameters of a constitutive model have been estimated, the quality of the least-squares approximation is evaluated by means of the R^2 value (Brown, 2001) defined as:

$$R^2 = 1 - \frac{\sum_{i=1}^{n_s}\left(\mathcal{T}_i - \mathcal{T}(\lambda_r^i)\right)^2}{\sum_{i=1}^{n_s}\left(\mathcal{T}_i - \overline{\mathcal{T}}\right)^2}, \tag{24}$$

where n_s is the number of strain–stress experimental measurements $(\lambda_r^i\ ,\ \mathcal{T}_i)$, for $i = 1, \ldots, n_s$, $\overline{\mathcal{T}}$ is the mean measured membrane tension, and $\mathcal{T}(\lambda_r^i)$ is the membrane tension evaluated at the measured deformation λ_r^i. The closer to one is the R^2 value corresponding to a constitutive model, the better is the data fitting.

Sections 2.3.1 and 2.3.2 present the functions $\mathcal{T}(\lambda_r)$ used to approximate the experimental measurements for the constitutive models of Section 2.2.2 together with the values of the selected material parameters and the corresponding R^2 values. We recall that, as discussed in Section 2.2.1, the penalization parameter κ in Eq. (7) is not involved in the parameter estimation procedure; we set $\kappa = 9.0\times10^6$ dyn/cm^2.

2.3.1. Determination of the parameters for isotropic materials

For isotropic models, under the incompressibility assumption (i.e. $J = 1$), Eq. (5) reduces to

$$\mathcal{W} = \overline{\mathcal{W}}_{iso}(\bar{I}_1, \bar{I}_2) = \mathcal{W}_{iso}(I_1, I_2). \tag{25}$$

According to Wulandana and Robertson (2005), the strain–stress function $\mathcal{T} = \mathcal{T}(\lambda_r)$ for the data fitting is

$$\mathcal{T}(\lambda_r) = \frac{h}{\lambda_r}\left(\lambda_r^2 - \frac{1}{\lambda_r^2}\right)\left(2\frac{\partial \mathcal{W}_{iso}}{\partial I_1} + 2\frac{\partial \mathcal{W}_{iso}}{\partial I_2}\right) \tag{26}$$

for each of the constitutive models of Section 2.2.3 ($\mathcal{W}_{iso}^{SVK}$, $\mathcal{W}_{iso}^{EXP1}$, and $\mathcal{W}_{iso}^{EXP2}$). Fig. 3(a) shows the least-squares approximation of the experimental data of (Scott et al., 1972) by means of the function $\mathcal{T} = \mathcal{T}(\lambda_r)$ for each of the isotropic constitutive models with the material parameters of Table 1. As indicated by the R^2 value in Table 1, in the case of the SVK model the experimental data are not properly approximated on the full range of transmural pressures. Conversely, the data fitting improves when the EXP1 and EXP2 models are considered. In these cases, as shown in Fig. 3(a), for transmural pressures higher than 50 mmHg, small differences are observed between the two approximated strain–stress relations. On the other hand, see Fig. 3(b), for low transmural pressures, the second order exponential (EXP2) model provides the best approximation of the data with respect to the other two isotropic model.

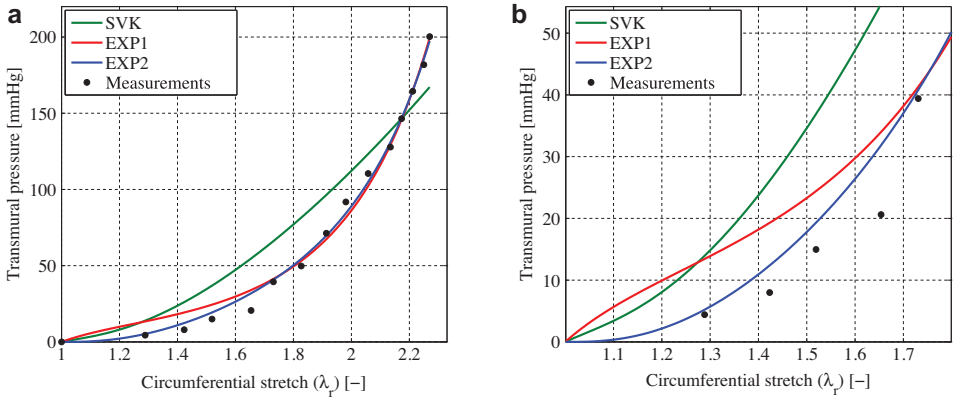

Fig. 3. Least-squares approximation of the data in Scott et al. (1972) using the isotropic models. Full range of transmural pressures $\Delta P \in [0, 200]$ mmHg (left); low transmural pressures regime $\Delta P \in [0, 40]$ mmHg (right).

2.3.2. Determination of the parameters for anisotropic materials

Similarly to Eq. (25), under the incompressibility assumption (i.e. $J = 1$), Eq. (20) reduces to:

$$\mathcal{W} = \overline{\mathcal{W}}_{aniso}(\bar{I}_1, \bar{I}_2, \bar{\mathbf{I}}_4, \bar{\mathbf{I}}_5) = \mathcal{W}^{bg}_{aniso}(I_1, I_2) + \mathcal{W}^{fibers}_{aniso}(\mathbf{I}_4, \mathbf{I}_5). \tag{27}$$

As in other works where anisotropic models describe the arterial tissue (e.g. Balzani et al., 2006a; Balzani et al., 2012; Dalong & Robertson, 2009), we consider two families of collagen fibers oriented symmetrically with respect to the circumferential direction of the cylinder as in Fig. 2. In addition, we remark that, for anisotropic models, the material parameters $\alpha^{(i)}$ and $\gamma^{(i)}$ in Eq. (19) are the same for all families of fibers. According to Dalong and Robertson (2009), for the anisotropic models of Section 2.2.4 the function $\mathcal{T} = \mathcal{T}(\lambda_r)$ reads as:

$$\mathcal{T}(\lambda_r) = \frac{h}{\lambda_r}\left[2\left(\lambda_r^2 - \frac{1}{\lambda_r^2}\right)\frac{\partial \mathcal{W}^{bg}_{aniso}}{\partial I_1} + \sum_{i=1}^{2} 2\frac{\partial \mathcal{W}^{fibers,(i)}_{aniso}}{\partial I_4^{(i)}}\frac{\lambda_r^2 \cos^2\beta^{(i)}}{\|\boldsymbol{a}_A^{(i)}\|^2}\right], \tag{28}$$

where $\beta^{(i)}$ is the angle between the characteristic direction of the ith fiber family in the reference configuration $\mathcal{B}_0$, indicated by $\mathbf{a}_0^{(i)}$, and the circumferential axis $\mathbf{e}_\theta$ (see Fig. 2). We remark that in Eq. (28), due to the representation of the arterial tissue as a membrane, the recruitment of the collagen fibers will occur simultaneously throughout the thickness of the vessel wall (Wulandana & Robertson, 2005). In addition, we set $\beta^{(1)} = -\beta^{(2)}$ and $\|\boldsymbol{a}_A^{(1)}\|^2 = \|\boldsymbol{a}_A^{(2)}\|^2$. In order to include in the least-squares approximation the activation condition ($I_4^{(i)} > \|\boldsymbol{a}_A^{(i)}\|^2$) of Eq. (21) we consider the following modified form of Eq. (28):

$$\mathcal{T}(\lambda_r) = \frac{h}{\lambda_r}\left[2\left(\lambda_r^2 - \frac{1}{\lambda_r^2}\right)\frac{\partial \mathcal{W}^{bg}_{aniso}}{\partial I_1} + \sum_{i=1}^{2}\left(\frac{1}{\pi}\arctan(\epsilon(I_4^{(i)} - \|\boldsymbol{a}_A^{(i)}\|^2)) + \frac{1}{2}\right)2\frac{\partial \mathcal{W}^{fibers,(i)}_{aniso}}{\partial I_4^{(i)}}\frac{\lambda_r^2 \cos^2\beta^{(i)}}{\|\boldsymbol{a}_A^{(i)}\|^2}\right], \tag{29}$$

to relate the membrane tension to the circumferential stretch. The activation stretch $\|\boldsymbol{a}_A^{(i)}\|^2$ depends on the angle $\beta^{(i)}$ and on the circumferential stretch ($\lambda_r^{A,(i)}$) at which the recruitment of the ith family of collagen fibers occurs by means of the relation (Dalong & Robertson, 2009):

$$\|\boldsymbol{a}_A^{(i)}\|^2 = (\lambda_r^{A,(i)})^2 \cos^2\beta^{(i)} + \sin^2\beta^{(i)}, \tag{30}$$

and we set $\lambda_r^{A,(1)} = \lambda_r^{A,(2)}$. As discussed in Section 2.2.4 we consider anisotropic models for which the collagen fibers are activated when their deformed length is either greater than their length in the reference configuration $\|\boldsymbol{a}_0^{(i)}\|$ or greater than a reference length $\|\boldsymbol{a}_{MM}^{(i)}\|$. In the first case (EXP2-RCmodel) such assumption implies that $\lambda_r^{A,(i)} = 1$ and therefore $\|\boldsymbol{a}_A^{(i)}\|^2 = \|\boldsymbol{a}_0^{(i)}\|^2 = 1$, for $i = 1, 2$. Conversely, for the multi-mechanism model (EXP2-MMmodel) $\lambda_r^{A,(i)} > 1$ and, therefore, $\|\boldsymbol{a}_A^{(i)}\|^2 > 1$, for $i = 1, 2$, Dalong (2009). In Dalong and Robertson (2009); Wulandana and Robertson (2005) an estimation of the circumferential stretch of activation in Eq. (30) is provided based on the measurements reported in Scott et al. (1972). However, since no experimental observations on the circumferential stretch of activation were reported in Scott et al. (1972), we consider $\lambda_r^{A,(1)}$ as an additional material parameter to be estimated for the EXP2-MMmodel.

As discussed in Section 2.2.4, we employ either the EXP1 or EXP2 model to describe the mechanical behavior of the background material. In the following, an anisotropic model will be indicated by the couple of strain energy functions used for the background material and the collagen fibers. Table 2 summarizes the material parameters and R^2 value for each of the anisotropic models under consideration. In Table 2, (α^{bg}, γ^{bg}) represent the material parameters characterizing the

Table 2
Parameters for the anisotropic models. α^{bg}_{aniso}, $\alpha^{(1)}$ [dyn/cm^2]; $\beta^{(1)}$ [rad]; γ^{bg}_{aniso}, $\gamma^{(1)}$, $\lambda_r^{A,(1)}$ [−].

Model ($\mathcal{W}_{aniso}$)	Material parameters	R^2
$\mathcal{W}^{EXP1}_{aniso} + \mathcal{W}^{EXP2\text{-}RC}_{aniso}$	$\alpha^{bg}_{aniso} = 1.7471\times10^4$, $\gamma^{bg}_{aniso} = 0.8620$ $\alpha^{(1)} = 1.4979\times10^5$, $\gamma^{(1)} = 0.5736$ $\beta^{(1)} = 0.9865$	0.9951
$\mathcal{W}^{EXP2}_{aniso} + \mathcal{W}^{EXP2\text{-}RC}_{aniso}$	$\alpha^{bg}_{aniso} = 6.8220\times10^4$, $\gamma^{bg}_{aniso} = 0.8620$ $\alpha^{(1)} = 6.008\times10^{-6}$, $\gamma^{(1)} = 0.8211$ $\beta^{(1)} = 1.4984$	0.9971
$\mathcal{W}^{EXP1}_{aniso} + \mathcal{W}^{EXP2\text{-}MM}_{aniso}$	$\alpha^{bg}_{aniso} = 3.5270\times10^4$, $\gamma^{bg}_{aniso} = 0.3424$ $\alpha^{(1)} = 1.3370\times10^5$, $\gamma^{(1)} = 0.2141$ $\beta^{(1)} = 0.7473$, $\lambda_r^{A,(1)} = 1.5009$	0.9980
$\mathcal{W}^{EXP2}_{aniso} + \mathcal{W}^{EXP2\text{-}MM}_{aniso}$	$\alpha^{bg}_{aniso} = 5.5420\times10^4$, $\gamma^{bg}_{aniso} = 3.0\times10^{-4}$ $\alpha^{(1)} = 1.3087\times10^5$, $\gamma^{(1)} = 0.5133$ $\beta^{(1)} = 0.8251$, $\lambda_r^{A,(1)} = 1.6538$	0.9985

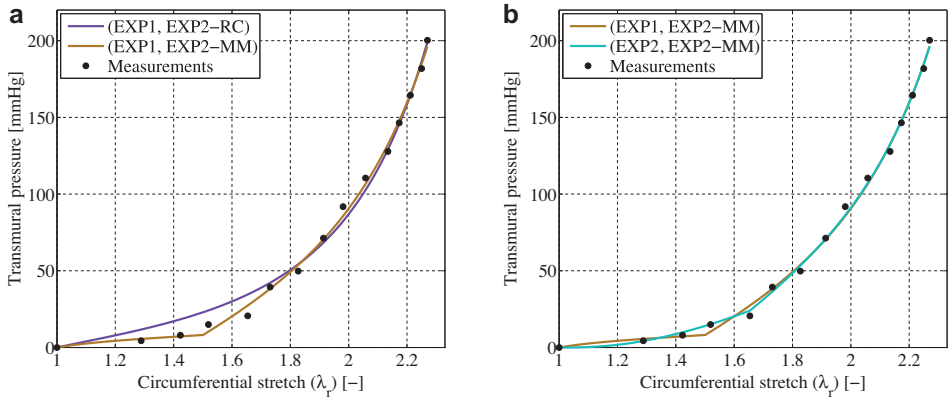

Fig. 4. Least-squares approximation of the data in Scott et al. (1972) using the anisotropic models.

background material while ($\alpha^{(1)}$, $\gamma^{(1)}$, $\beta^{(1)}$, $\lambda_r^{A,(1)}$) are the material parameters for the single family of collagen fibers. We remark that the least-squares approximation of the data improves when anisotropic models are used with respect to isotropic models (Table 1). In addition, when the multi-mechanism model describes the collagen fibers the approximation of the experimental data is further improved with respect to the EXP2-RCmodel. Fig. 4(a) shows the membrane tension $\mathcal{T}(\lambda_r)$ for the (EXP1, EXP2-RC) and (EXP1, EXP2-MM) models. Fig. 4(b) shows the function $\mathcal{T}(\lambda_r)$ when either the EXP1 or the EXP2 models describe the background material and the collagen fibers are represented by the EXP2-MMmodel. In this case, the estimation of the circumferential stretch of activation $\lambda_r^{A,(1)}$ is strongly affected by the choice of the model for the background material (see Fig. 4(b) and Table 2). This is due to the fact that, as shown in Fig. 3(b), the EXP2 model fits better than the EXP1 law the data in the low pressure regime; therefore, when using the EXP2 model for the background material, the collagen fibers are activated at a higher activation circumferential stretch in order to fit the high transmural pressure regime.

We observe that, in Fig. 4(a) and (b), the recruitment of the collagen fibers at finite strains induces the sharp change in the membrane tension $\mathcal{T}(\lambda_r)$ around the circumferential stretch of activation $\lambda_r^{A,(1)}$. Although the (EXP2, EXP2-MM) model gives the best least-squares approximation of the experimental measurement, it will not be employed in the numerical simulations of healthy cerebral arterial tissue due to numerical issues related to the numerical solution of the structural mechanics problem (3) (Tricerri, 2014). The fact that the highest R^2 values are obtained in the case of anisotropic models, for which the number of parameters is higher than the one of the isotropic laws, stresses the importance of experimental observations on the properties of the collagen fibers in terms of their spatial orientation and activation stretch (Hill, Duan, Gibson, Watkins, & Robertson, 2012). Indeed, when a large number of parameters needs to be estimated by means of the least-squares data fitting of experimental measurements (Odgen, Saccomandi, & Sgura, 2004), non-uniqueness issues may arise. These effects are mitigated when some parameters of the material model are known a priori; for example, in the case of anisotropic models, these may be the properties of the collagen fibers.

2.4. Mathematical modeling of elastin weakening

As described in Section 1, the onset of diseases such as atherosclerosis or cerebral aneurysms, is related to the mechanical degradation of the mechanical properties of the elastin of the arterial tissue. We describe the weakening of the arterial tissue that occurs in diseased states of arteries (e.g. during the early phases of the formation of a cerebral aneurysm) by means of an isotropic damage model. Following the approach proposed in Kachanov (1958); Skrzypek and Ganczarski (1999), a dimensionless weakening parameter $D \in [0, 1)$ is used to represent the level of mechanical weakening affecting the material. The unhealthy arterial tissue is then described by means of one of the constitutive models described in Section 2.2.2 for which the parameter representing the mechanical stiffness of the material is reduced by a factor of D. The arterial tissue is healthy and its mechanical properties intact when $D = 0$, while its full mechanical failure occurs when $D \to 1$. We remark that the approach of (Kachanov, 1958; Skrzypek & Ganczarski, 1999) is commonly employed in literature when the mechanical degradation of the arterial tissue is described at the macroscopic scale as a function of either hemodynamical or chemical factors, as done in e.g. Calvo et al. (2007); Dalong et al. (2012); Famaey, Sommer, Stolen, and Holzapfel (2012); Li and Robertson (2009); Weisbecker, Pierce, and Holzapfel (2011). However, we point out that there is a general lack of experimental measurements on weakened arterial tissue that can be used to validate the mathematical damage models proposed for unhealthy tissues in Calvo et al. (2007); Dalong et al. (2012); Famaey et al. (2012); Li and Robertson (2009); Weisbecker et al. (2011).

As discussed in Section 2.1 the choice of the isochoric strain energy function $\overline{\mathcal{W}}$ (either isotropic or anisotropic) characterizes the mathematical description of the arterial tissue. When describing an unhealthy state of the arterial tissue, the weakening factor $(1 - D)$ affects only the isochoric part in the additive decomposition of the strain energy function (see Eq. (5)). Therefore, when using isotropic laws to model the unhealthy vessel wall, Eq. (5) is transformed as follows:

$$\mathcal{W}_{iso}(J, \bar{I}_1, \bar{I}_2; D) = \mathcal{U}(J) + \overline{\mathcal{W}}_{iso}(\bar{I}_1, \bar{I}_2; D). \tag{31}$$

When the vessel wall is described by the anisotropic model of Eq. (21), the weakening factor could affect the strain energy for the background material $\overline{\mathcal{W}}^{bg}_{aniso}$ and the one describing the collagen fibers $\overline{\mathcal{W}}^{fibers}_{aniso}$ in Eq. (14), or only one of the two. Based on the experimental observations on cerebral aneurysms, for which only the elastin is degraded in the early stages development of cerebral aneurysms, we assume that the weakening model affects only the mechanical contribution provided by the isotropic part $\overline{\mathcal{W}}^{bg}_{aniso}$ of the strain energy function in Eq. (21). According to this choice, the anisotropic constitutive model for the unhealthy vessel wall reads:

$$\mathcal{W}_{aniso}(J, \bar{I}_1, \bar{I}_2, \bar{\mathbf{I}}_4, \bar{\mathbf{I}}_5; D) = \mathcal{U}(J) + \overline{\mathcal{W}}^{bg}_{aniso}(\bar{I}_1, \bar{I}_2; D) + \overline{\mathcal{W}}^{fibers}_{aniso}(\bar{\mathbf{I}}_4, \bar{\mathbf{I}}_5). \tag{32}$$

In Balzani (2006); Balzani et al. (2006b); Dalong (2009); Dalong and Robertson (2009) the weakening parameter D is a function of kinematics quantities that depend on the history of the deformations that occur during the motion of the body, such as the maximum deformation or the maximum value of elastic energy (Balzani, 2006; Dalong, 2009). We are interested in analyzing the influence on kinematics quantities of interest for the modeling of unhealthy cerebral arterial tissue of isotropic and anisotropic constitutive models at different levels of mechanical weakening of the arterial tissue. For this reason, we fix a priori different values for D in the constitutive models of Eqs. (31) and (32). In order to have consistent comparisons among the different numerical simulations, it is necessary to calibrate the weakening parameter D for the different constitutive models; we detail this aspect in Section 2.5.

2.5. Calibration of the weakening parameter D for unhealthy cerebral arterial tissue

Based on the results obtained from the least-squares approximation of the experimental data, we represent the unhealthy cerebral arterial tissue by introducing the weakening parameter D in three of the constitutive models discussed in Section 2.2.2: the isotropic EXP2 model, and the anisotropic models (EXP1, EXP2-RC) and (EXP1, EXP2-MM). The weakening parameter D is introduced in the constitutive models by means of the factor $(1 - D)$ multiplying the material parameters representing the mechanical stiffness of the material. Thus, the isochoric term $\overline{\mathcal{W}}_{iso}$ in Eq. (31) for the isotropic EXP2 model (indicated as U-EXP2) reads as:

$$\overline{\mathcal{W}}_{iso}(\bar{I}_1, \bar{I}_2; D) = \overline{\mathcal{W}}^{U\text{-}EXP2}_{iso}(\bar{I}_1, \bar{I}_2; D_{EXP2}) = \frac{(1 - D_{EXP2})\alpha_2}{2\gamma_2}\left(e^{\gamma_2(\bar{I}_1 - 3)^2} - 1\right). \tag{33}$$

The weakened background material in the anisotropic models is described by the following modified form of the EXP1 model (indicated as U-EXP1):

$$\overline{\mathcal{W}}^{bg}_{aniso}(\bar{I}_1, \bar{I}_2; D) = \overline{\mathcal{W}}^{U\text{-}EXP1}_{iso}(\bar{I}_1, \bar{I}_2; D_{EXP1}) = \frac{(1 - D_{EXP1})\alpha^{bg}_{aniso}}{2\gamma^{bg}_{aniso}}\left(e^{\gamma^{bg}_{aniso}(\bar{I}_1 - 3)} - 1\right). \tag{34}$$

In the following, the anisotropic models for unhealthy cerebral arterial tissue will be indicated as (U-EXP1, EXP2-RC) and (U-EXP1, EXP2-MM), respectively, and $D^{EXP2\text{-}RC}_{EXP1}$ and $D^{EXP2\text{-}MM}_{EXP1}$ will represent the weakening parameter affecting the material properties of the background material in the (U-EXP1, EXP2-RC) and (U-EXP1, EXP2-MM), respectively. As pointed out in Section 2.4, the mechanical weakening of the tissue affects only the mechanical properties of the background material

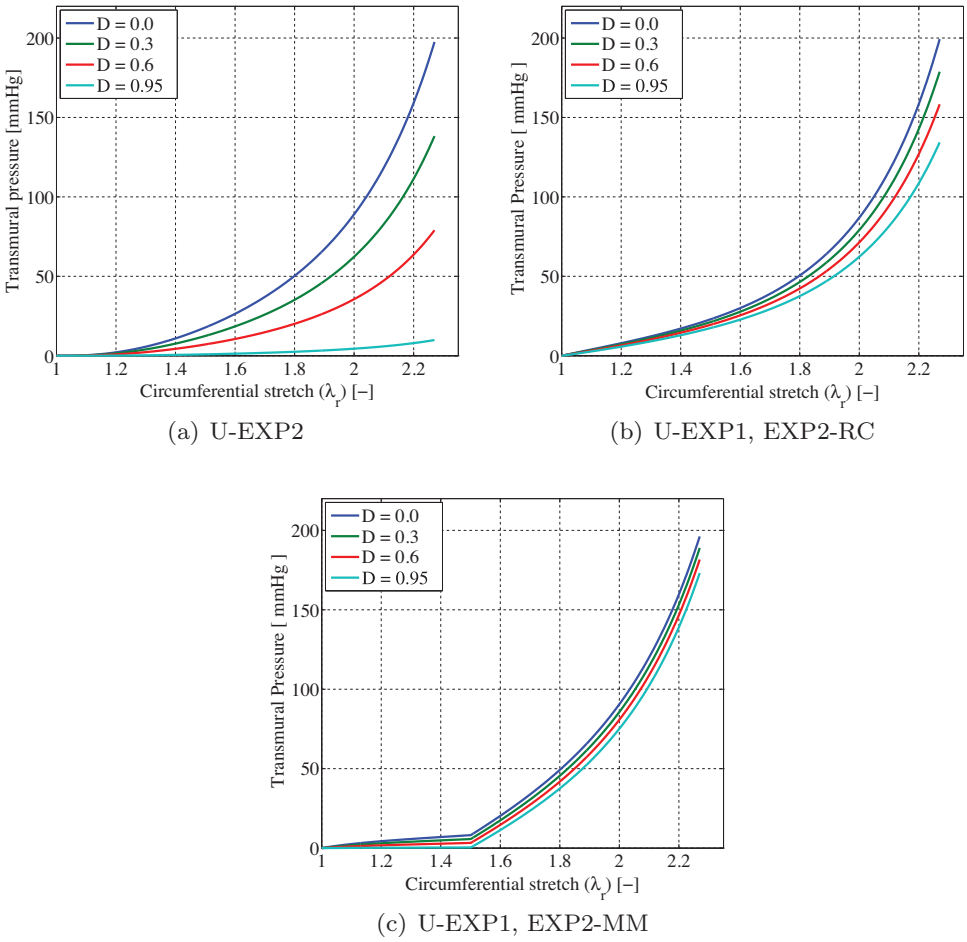

Fig. 5. Functions $\mathcal{T}(\lambda_r)$ for different values of the weakening parameter D.

Table 3
Values for the weakening parameter D used in the numerical simulations.

Case	Weakening parameter D
1	$D_{ref} = D_{EXP1}^{EXP2\text{-}MM} = 0.7500$, $D_{EXP1}^{EXP2\text{-}RC} = 0.3010$, $D_{EXP2} = 0.1103$
2	$D_{ref} = D_{EXP1}^{EXP2\text{-}RC} = 0.6000$, $D_{EXP2} = 0.2641$

(Eq. (32)). Although different constitutive models can be adjusted to a set of experimental measurements in order to represent the healthy cerebral arterial tissue (Section 2.3), the choice of the weakening parameter D in Eqs. (33) and (34) has an important effect on the characterization of unhealthy cerebral arterial tissues. Fig. 5 shows the strain–stress functions $\mathcal{T}(\lambda_r)$ of Figs. 3(a) and 4(a) for the EXP2, (EXP1, EXP2-RC) and (EXP1, EXP2-MM) models for different values of the weakening parameter D. We observe that, for $D > 0.6$ the three curves do not intersect in the physiological range of transmural pressures ($\Delta P \in [70, 150]$). For this reason, the proper calibration of the weakening parameter D according to the model describing the vessel wall is necessary. We have calibrated the values of the parameter D for the three constitutive models with respect to a reference value for D_{ref} and the reference transmural pressure $\Delta P_{ref} = 110$ mmHg. More specifically, we have considered two cases. Firstly, we have fixed $D_{ref} = D_{EXP1}^{EXP2\text{-}MM} = 0.75$ for the (U-EXP1, EXP2-MM) model and determined the values of D_{EXP2} and $D_{EXP1}^{EXP2\text{-}RC}$ for the remaining two models such that the three functions $\mathcal{T} = \mathcal{T}(\lambda_r)$ intersect at the reference transmural pressure ΔP_{ref}. Then, we followed the same approach considering $D_{ref} = D_{EXP1}^{EXP2\text{-}RC} = 0.6$ for the (U-EXP1, EXP2-RC). We remark that in the latter case, as shown in Fig. 5(c), it is not possible to find a value of $D \in [0, 1)$ for which the (U-EXP1, EXP2-MM) model yield the reference deformation at the reference pressure. Fig. 6 shows the functions $\mathcal{T} = \mathcal{T}(\lambda_r)$ for the three constitutive models under consideration with the material parameters of Tables 1 and 2 and the values of the weakening parameter D summarized in Table 3.

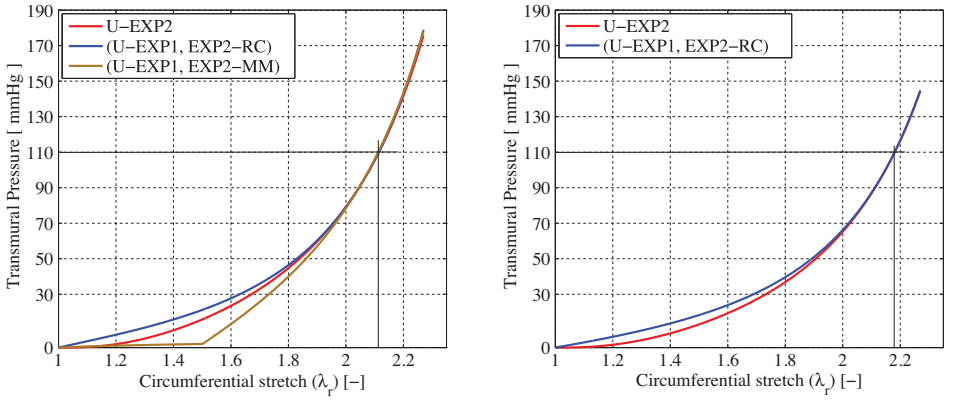

(a) Case 1. (b) Case 2

Fig. 6. Functions $\mathcal{T}(\lambda_r)$ with the weakening parameters of Table 3.

3. Numerical approximation: the Finite Element method

Problem (3) is solved by means of the Finite Element method (Quarteroni & Valli, 1999b). With this aim, let us introduce the Hilbert space V of functions $V(\mathcal{B}_0) = [H^1_{\Gamma_D}(\mathcal{B}_0)]^3 = \left\{ \boldsymbol{\psi} \in [H^1(\mathcal{B}_0)]^3 \text{ s.t. } \boldsymbol{\psi} = \mathbf{0} \quad \text{on } \Gamma_D \right\}$, for which the weak formulation of problem (3) reads :

find $\boldsymbol{d} = \boldsymbol{d}(\boldsymbol{X}) \in V$:

$$\int_{\mathcal{B}_0} \boldsymbol{P}(\boldsymbol{d}) : \nabla \boldsymbol{\psi} \; d\mathcal{B}_0 = \oint_{\Gamma_{in}} -p\boldsymbol{n} \cdot \boldsymbol{\psi} \; d\Gamma_{in} \quad \forall \boldsymbol{\psi} \in V. \tag{35}$$

The discrete problem is obtained by approximating the reference configuration $\mathcal{B}_0$by $\mathcal{B}_0^h$, a conforming mesh (triangulation) of $\mathcal{B}_0$, and by considering a finite dimensional subspace $V_h = (X_h^p \cap V) \subset V$ composed of Lagrangian, piecewise continuous polynomial basis functions of local polynomial degree $p \geq 1$ defining the space (X_h^p). Let $\{\boldsymbol{\psi}_A\}_{A=1}^{N_h}$, where $N_h := \dim(V_h)$, be the Lagrangian basis of V_h, in the form $\boldsymbol{\psi}_A = (\phi_A \mathbf{e}_1 + \phi_A \mathbf{e}_2 + \phi_A \mathbf{e}_3)$, where ϕ_A is a scalar Lagrangian function of V_h defined on the mesh $\mathcal{B}_0^h$, and $(\mathbf{e}_1, \mathbf{e}_2, \mathbf{e}_3)$ is the Euclidean base in $\mathbb{R}^3$. The discrete weak formulation of problem (3) is given by:

find $\boldsymbol{d}_h = \boldsymbol{d}_h(\boldsymbol{X}) = \sum_{A=1}^{N_h} \sum_{j=1}^{3} (d_{h,j})_A \phi_A(\boldsymbol{X}) \mathbf{e}_j \in V_h$:

$$\int_{\mathcal{B}_0^h} \boldsymbol{P}(\boldsymbol{d}_h) : \nabla \boldsymbol{\psi}_A \; d\mathcal{B}_0^h = \oint_{\Gamma_{in}^h} -p_h \boldsymbol{n} \cdot \boldsymbol{\psi}_A \; d\Gamma_{in}^h \quad \forall \boldsymbol{\psi}_A \in V_h, \tag{36}$$

where the jth component of the displacement field is defined as $d_{h,j} = \sum_{A=1}^{N_h} (\boldsymbol{d}_{h,j})_A \phi_A$, with $j = 1, 2, 3$. In Eq. (36), Γ_{in}^h is the approximation of the internal surface Γ_{in} provided by the mesh $\mathcal{B}_0^h$, and p_h is a suitable approximation of the boundary data p on Γ_{in} (e.g. the L^2-projection of p onto $X_h^p(\Gamma_{in})$).

We remark that the nonlinear constitutive relations considered in this work lead to the nonlinear problem (36) which is solved by means of the Newton method (Quarteroni et al., 2007). In order to guarantee the convergence of the Newton method for the values of transmural pressures of interest, we use a pseudo-time approach, for which the inflating pressure is gradually applied by using a pseudo-time function $p(t)$, represented in Fig. 7. At each iteration of the Newton method, Eq. (36) is linearized with respect to the displacement field $\boldsymbol{d}$ (see Balzani, 2006; Holzapfel, 2000) for which the tangent matrix ($J_{\boldsymbol{P}} = \frac{d\boldsymbol{P}(\boldsymbol{d})}{d\boldsymbol{d}}$) of the first Piola–Kirchhoff tensor $\boldsymbol{P}(\boldsymbol{d})$ is evaluated, and the resulting linear system is solved by means of the GMRES method (Saad, 1986) preconditioned with the Additive-Schwarz method (Quarteroni & Valli, 1999a).

4. Numerical validation

We numerically validate the constitutive models described in Section 2.2.2, for which the material parameters are reported in Tables 1 and 2. Firstly, we show results of numerical simulations of static inflation tests on healthy cerebral arterial tissue. Then, the weakening model discussed in Section 2.4 is considered and numerical simulations on unhealthy cerebral arterial tissue are discussed. Finally we report and discuss numerical results obtained from fluid–structure interaction simulations applied to patient-specific cerebral aneurysm. In this latter case, we compare results obtained with different isotropic constitutive laws.

The computational domain representing the cerebral artery (see Fig. 1) is discretized by a tetrahedral mesh composed of 384,000 elements with $\mathbb{P}1$Lagrangian finite elements for which the total number of degrees of freedom (DOFs) when approximating Eq. (36) is 241,200. The constitutive material models have been implemented in the finite element library

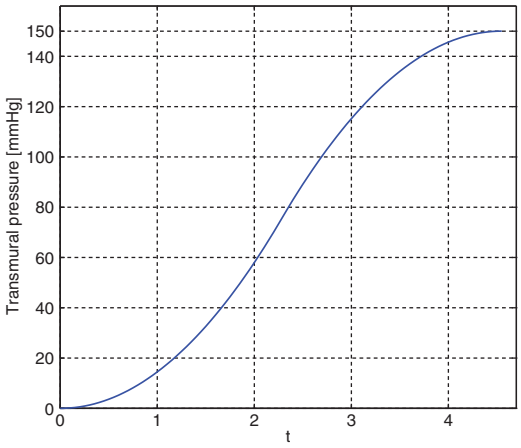

Fig. 7. Inflating pseudo-time pressure profile $p(t)$ for problem (3).

LifeV (LifeV, 2010) by means of an expression template assembly framework (Quinodoz, 2012). The numerical simulations have been run in parallel on 128 processors on the Cray XE6 supercomputer *Monte Rosa* at the Swiss national supercomputing center CSCS in Lugano, Switzerland.

4.1. Inflation tests on healthy cerebral tissue

We report in Fig. 8 the magnitude of the displacement field at the cross section located at $z = 1$ cm for $\Delta P = 150$ mmHg for the constitutive models of Section 2.2.2. As expected, the contour lines of the displacement are concentric with the largest displacement occurring at the inner surface of the artery. The displacement magnitude in Fig. 8(a)–(e) has been rescaled in order to show the correct qualitative behavior of all the numerical solutions; Fig. 8(f) presents the radial displacement through the thickness of the vessel wall for all the constitutive models. Figs. 9 and 10 show the strain–stress relations resulting from the least-squares approximation of the experimental measurements (see Section 2.3) and the ones obtained by the numerical simulations for the isotropic and anisotropic models, respectively. We report the circumferential stretch λ_r at the internal radius of the domain in order to compare it with the experimental measurement presented in Scott et al. (1972). The circumferential stretch was obtained from the numerical results computing the magnitude of the displacement field on Γ_{in} at the cross section $z = 1$ cm such that the effects of Dirichlet boundary conditions applied on Γ_D (see Fig. 1(a)) are negligible.

For the SVK isotropic model, as observed in Fig. 9(a), with pressures $\Delta P \in [70, 150]$ the strain–stress relation obtained from the numerical simulations does not adequately reproduce the one predicted by the data fitting, especially for the high values of ΔP. Conversely, a good agreement between the numerical and least-squares fitted strain–stress relations is observed for the EXP1 and EXP2 models. Such difference among the isotropic models can be ascribed to the choice of the penalization parameter κ in Eq. (7). The larger is κ, the smaller is the body displacement under the action of external forces. Thus, a value for κ that represents a good compromise between the need to model the quasi-incompressible behavior of arteries and to obtain a meaningful displacement field for a certain constitutive model, e.g. the EXP1 and EXP2 models, may become inappropriate for another one, e.g. the SVK model. However, in this study, in order to have a consistent comparison of the numerical results among the different cases under consideration, the same value for the penalty parameter has been used in our numerical simulations.

Fig. 10 shows the strain–stress curves obtained from the least-squares approximation and numerical simulation for the (EXP1, EXP2-RC) and (EXP1, EXP2-MM) models respectively. We observe a good agreement between the simulated strain–stress relations and the corresponding functions $\mathcal{T}(\lambda_r)$. For the (EXP1, EXP2-RC) model the highest error occurs for high transmural pressures while for the multi-mechanism model, i.e. (EXP1, EXP2-MM), the two curves are overlapped. However, in the latter case, the highest error occurs around the activation circumferential stretch. As discussed in Section 2.3.2, this is due to the fact that, in the data fitting, due to the membrane modeling of the vessel wall, the recruitment of the collagen fibers occurs simultaneously throughout the thickness of the vessel wall; this assumption does not hold in the numerical simulations since the arterial wall is described as a full three dimensional model.

Fig. 11 shows the relative error between the function $\mathcal{T}(\lambda_r)$ and the ones obtained from the numerical simulations. In the range of physiological transmural pressures, the maximum relative error is around 4% and it is observed for the isotropic SVK model. However, from the strain–stress measurements presented in Scott et al. (1972), we can conclude that the relative error between the function $\mathcal{T}(\lambda_r)$ and the numerically simulated strain–stress relations is compatible with (that is within the same range as) the one affecting the experimental measurements in Scott et al. (1972). In the physiological range of pressures for the EXP1, EXP2 and the anisotropic models, the relative error is below 2.5% confirming the good approximation of the least-squares fitted strain–stress relation by the numerical simulations.

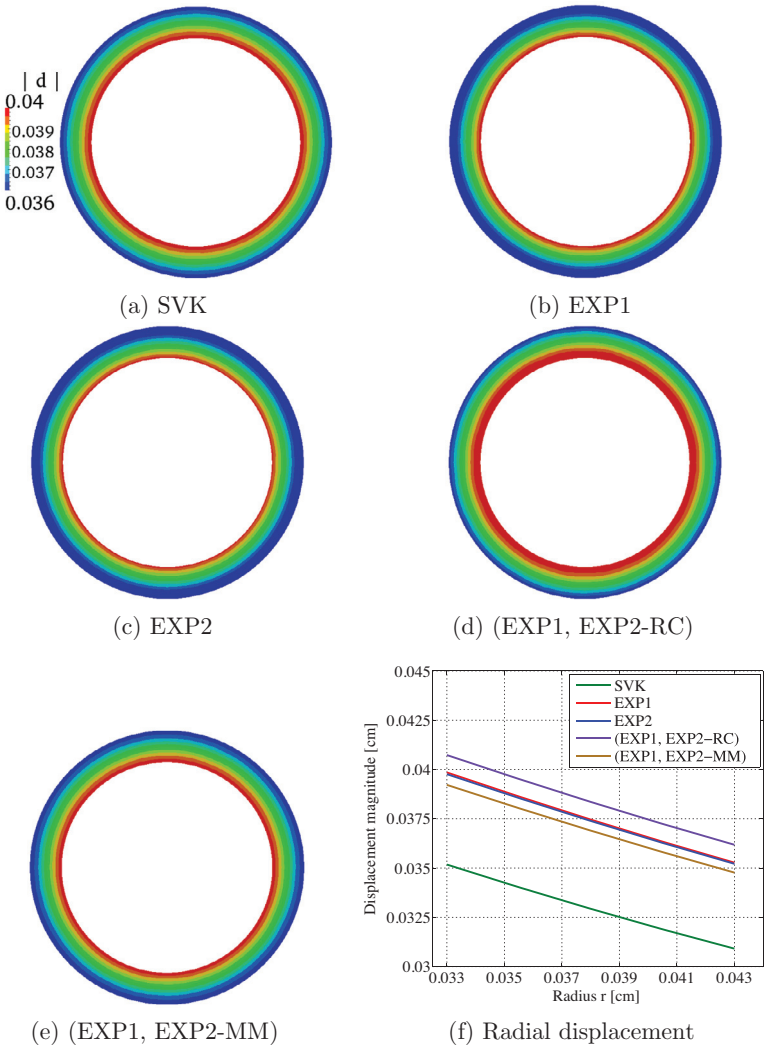

Fig. 8. Displacement magnitude [cm] at the cross section at $z = 1$ cm and $\Delta P = 150$ mmHg for different material models.

In the low pressures regime (i.e. for $\Delta P \in [0, 20]$ mmHg) the high relative errors are due to the use of linear finite elements for the discretization of Eq. (35) and they are observed for all the constitutive models. Indeed, from the numerical point of view, high values of the penalty parameter κ can lead to incorrect displacement fields or to locking phenomena when discretizing Eq. (35) by means of $\mathbb{P}1$finite elements (Brinkhues et al., 2013; Hughes, 2000). In this work, the value for κ has been set in order to simulate the nearly-incompressible behavior of blood vessels for $\Delta P \in [70, 150]$ mmHg; this may lead to displacements which are not circumferentially symmetric for low transmural pressures, as shown in Fig. 12 (left columns). However, such asymmetry can be addressed, for instance, by discretizing Eq. (35) by means of quadratic ($\mathbb{P}2$) finite elements, as shown in Fig. 12 (right columns). For this comparison we employ the isotropic EXP1 model and, in order to have the same number of DOFs with the quadratic elements as in the linear case, a new mesh with 49,896 elements and 234,360 DOFs has been considered. In Fig. 12 we observe that for $\Delta P \in [70, 150]$ mmHg, the use of $\mathbb{P}2$finite elements does not affect the circumferential stretch; therefore, we can conclude that the results presented in Figs. 9 and 10 are not significantly affected by the choice of the finite element space. Indeed, the vessel wall displacement on the internal surface of the domain is qualitatively equivalent when measured for the range of transmural pressures under consideration in the case of $\mathbb{P}1$and $\mathbb{P}2$finite element spaces. The results presented in Figs. 9 and 10 are slightly affected by the choice of the finite element space in the low pressure regime that, however, is not of interest in this work.

In order to highlight the influence of the bulk modulus on the approximation of the circumferential stretch, Fig. 13(a) shows the strain–stress relations obtained for different values of κ in Eq. (7) using the SVK model with the material parameters reported in Table 1. We observe the influence of the penalization parameter on the computed displacement field and we show that, in this case, a different value of κ (i.e. $\kappa = 4.0 \times 10^6$ dyn/cm^2) would have led to a better approximation of the function $\mathcal{T} = \mathcal{T}(\lambda_r)$ in the range of transmural pressures of interest (see Fig. 13(b)).

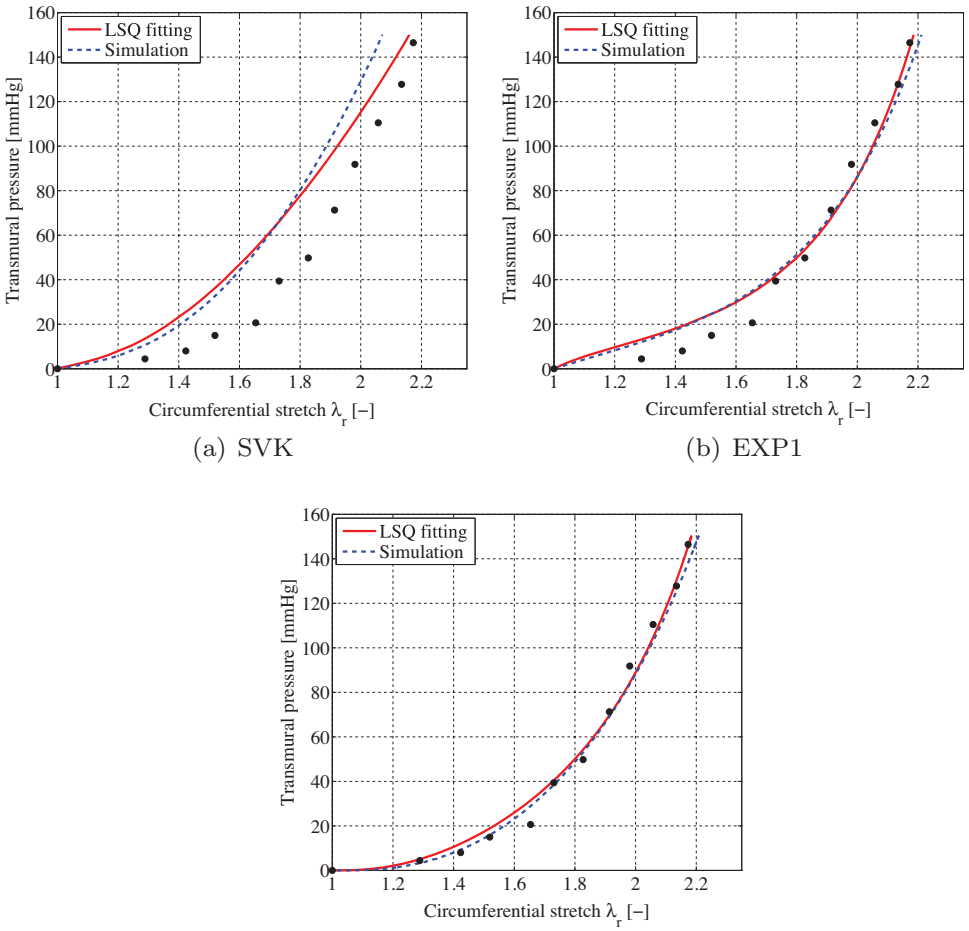

Fig. 9. Strain–stress relation $\mathcal{T}(\lambda_r)$ and corresponding relation obtained from the numerical simulations for the isotropic models of Section 2.2.2. The dots represent the experimental data in Scott et al. (1972).

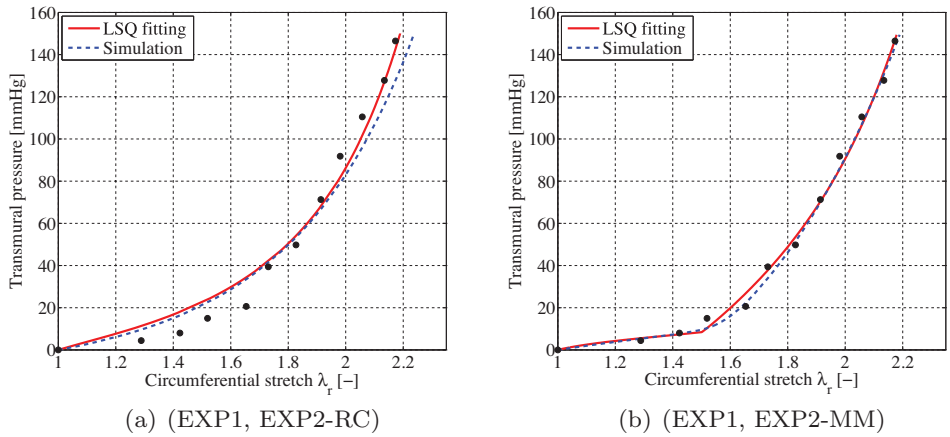

Fig. 10. Strain–stress relation $\mathcal{T}(\lambda_r)$ and corresponding relation obtained from the numerical simulations for the anisotropic models of Section 2.2.2. The dots represent the experimental data in Scott et al. (1972).

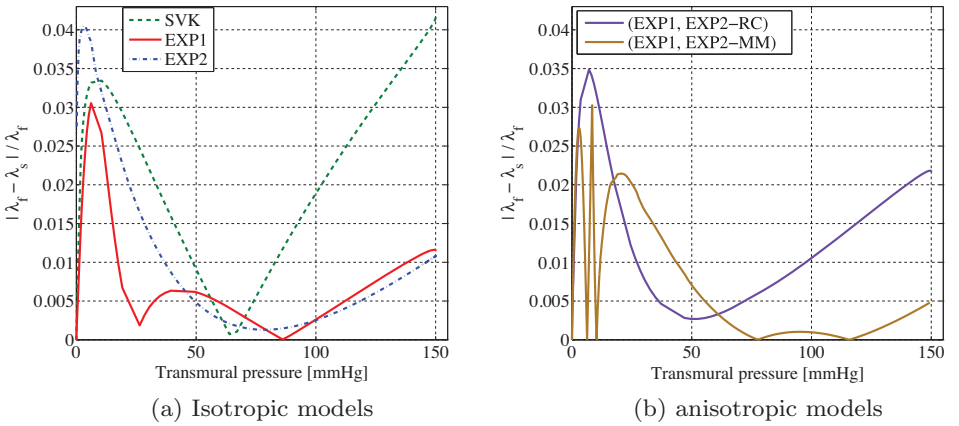

(a) Isotropic models (b) anisotropic models

Fig. 11. Relative error between the two strain–stress relations of Figs. 9 and 10 as a function of ΔP.

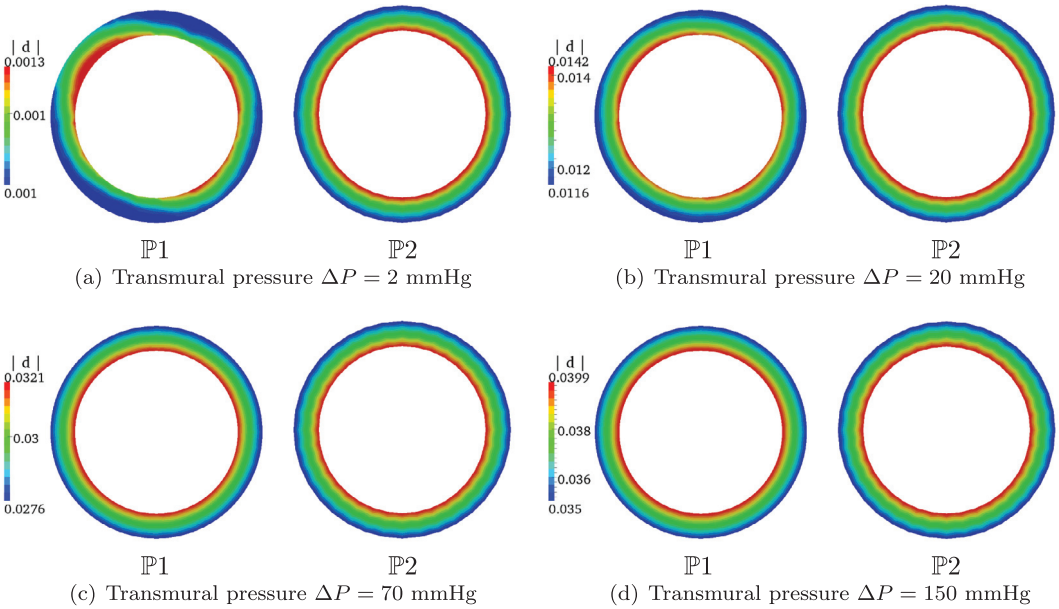

(a) Transmural pressure $\Delta P = 2$ mmHg (b) Transmural pressure $\Delta P = 20$ mmHg

(c) Transmural pressure $\Delta P = 70$ mmHg (d) Transmural pressure $\Delta P = 150$ mmHg

Fig. 12. Displacement magnitude [cm] at different inflating pressures using the isotropic EXP1 model: using $\mathbb{P}1$elements (#DOFs: 241,200) (left columns); using $\mathbb{P}2$elements (#DOFs: 234,360) (right columns).

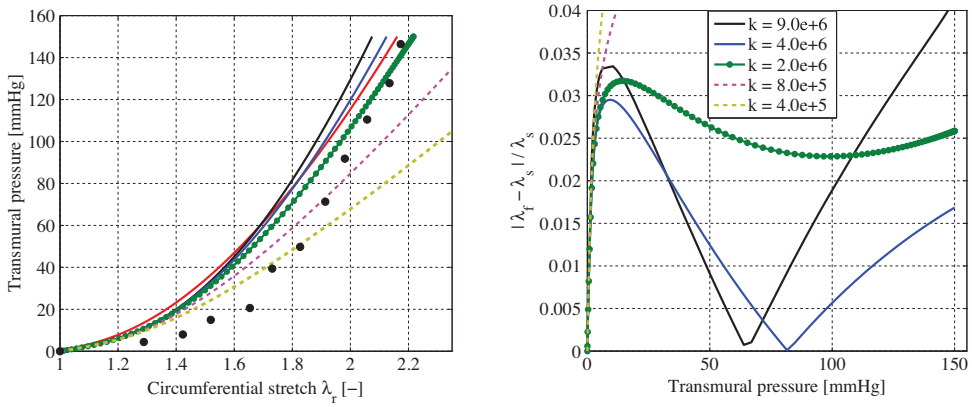

(a) Strain-stress relation (b) Relative error

Fig. 13. Strain–stress relations for different values of κ for the isotropic SVK model with the material parameters of Table 1.

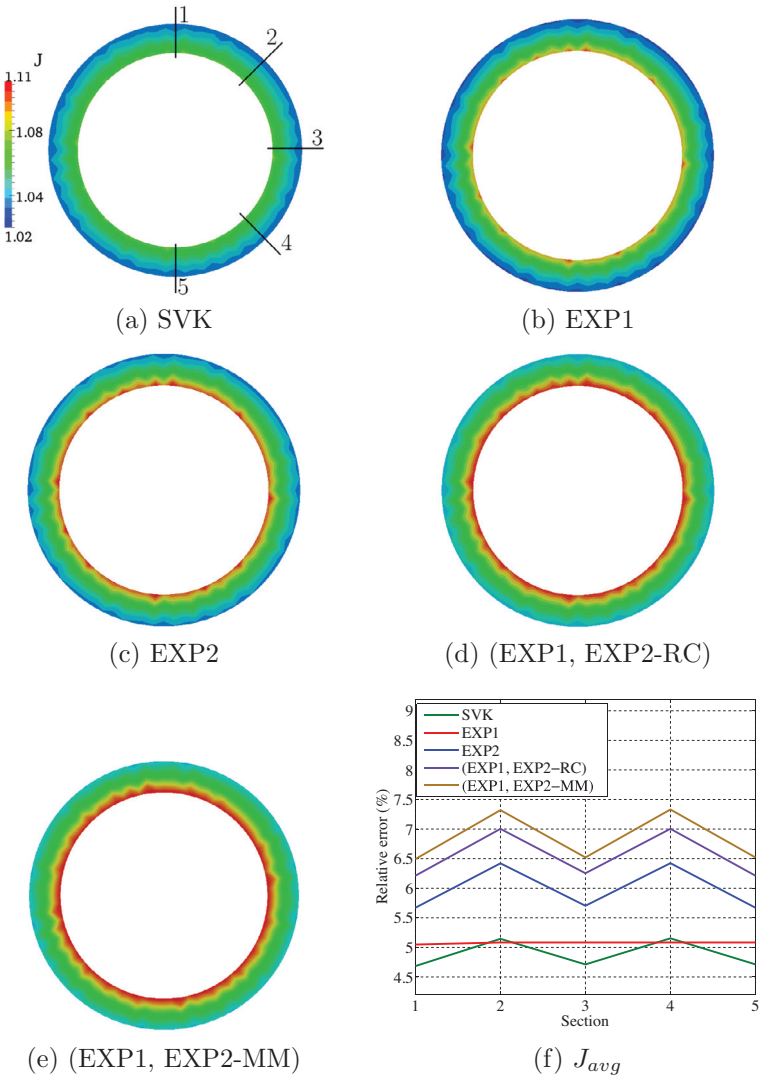

Fig. 14. Volume ratio J and J_{avg} at $z = 1$ cm, $\Delta P = 150$ mmHg for the different material models; $\kappa = 9.0\times10^6$ dyn/cm^2.

Fig. 14 shows the approximation of the incompressibility constraint at the cross section $z = 1$ cm at the inflating pressure of 150 mmHg for the constitutive models of Section 2.2.2. The largest error on the approximation of the volumetric constraint ($J = 1$) occurs at the internal surface of the artery where the displacement is higher. The smallest error, around 4.5%, is obtained for the SVK model due to the smaller radial displacement (see Fig. 9(a)) of the vessel with respect to those obtained with the other constitutive laws. As discussed for Fig. 13, the choice of the penalization parameter κ strongly affects the numerical results for the SVK model. Fig. 15 shows the Jacobian J at the cross section $z = 1$ cm at the inflating pressure of 150 mmHg for two different values of κ ($\kappa = 4.0\times10^6$ and $\kappa = 9.0\times10^6$ dyn/cm^2) using the SVK model. We remark that, in Fig. 15, the Jacobian J is presented only for the values of κ such that the error on the incompressibility constraint is lower than 20%. For the SVK model, Fig. 13(a) shows that for $\Delta P \in [70, 150]$ mmHg, $\kappa = 4.0\times10^6$ dyn/cm^2 leads to a better approximation of the strain–stress relation $\mathcal{T}(\lambda_r)$ by means of the numerical simulations; however, such choice for the penalization parameter yields a poor approximation of the incompressibility constraint. For the constitutive models of Section 2.2.2 the biggest error is reported for the anisotropic models, as in Fig. 14. Although the approximation of the kinematic constraint $J = 1$ is acceptable for all the constitutive laws under consideration, the numerical results indicate that a higher value of the penalization parameter κ in the volumetric strain energy function could be employed in the case of anisotropic models (Tricerri, 2014). This suggests that, once again, the value of the penalty parameter κ used for the numerical simulations should be tuned according to the constitutive law used to describe the tissue. Fig. 14(f) shows the relative error (percentage) on the incompressibility constraint for $\Delta P = 150$ mmHg. More specifically, in Fig. 14(f) the relative error is defined as $Er = 100(J_{avg} - 1)$, where J_{avg} is the average of the volume ratio along each one of the directions depicted in Fig. 14(a). The oscillations reported in Fig. 14(f) highlight the mesh dependence of the numerical results. Indeed, we observe

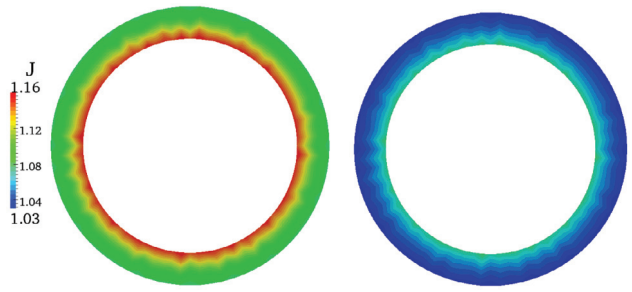

(a) $\kappa = 4.0 \cdot 10^6$ dyn / cm^2 (b) $\kappa = 9.0 \cdot 10^6$ dyn / cm^2

Fig. 15. Volume ratio J for different values of the penalization parameter κ for the SVK model at the pressure $\Delta P = 150$ mmHg.

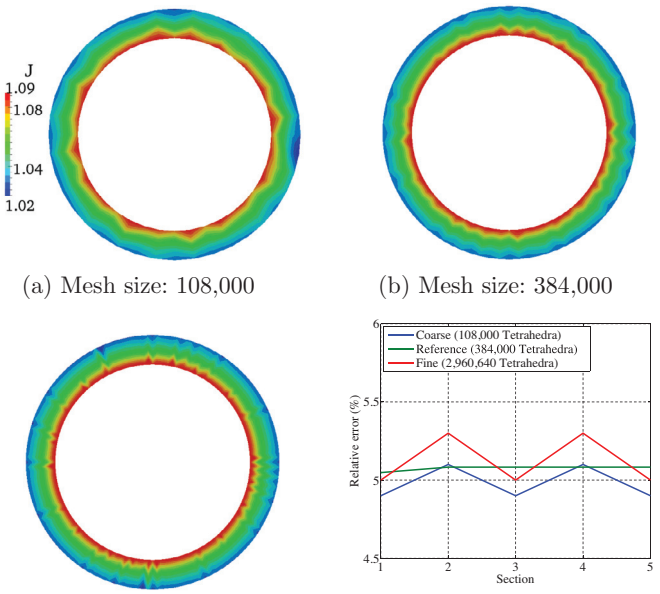

(a) Mesh size: 108,000 (b) Mesh size: 384,000

(c) Mesh size: 2,960,640 (d) Relative error

Fig. 16. Volume ratio J for different meshes of the computational domain.

that the Jacobian J in Fig. 14 is computed at the highest value of the transmural pressure for which the numerical solution obtained with linear and quadratic finite elements is the same. However, the Jacobian J depends on the spatial gradient of the displacement field, which in the case of Lagrangian basis function is strongly affected by the spatial orientation of the tetrahedra in the mesh. Thus, the oscillations in Fig. 14(f) cannot be addressed by employing $\mathbb{P}2$finite elements for the discretization of the weak formulation. The averaged Jacobians J_{avg} in Fig. 14(f) indicate that the value of κ used in the numerical simulations leads to an acceptable approximation of the incompressibility constraint with the maximum relative error being approximatively 7%.

In order to evaluate the mesh dependency on the approximation of the incompressibility constraint, numerical simulations of static inflation tests have been carried out for two additional meshes: one coarser and one finer than the reference mesh. For this numerical comparison, the tests have been carried out using the isotropic EXP1 model and $\mathbb{P}1$finite elements. The coarser mesh is composed of 108,000 elements while the finer one is composed of 2,960,640 tetrahedra, yielding to 72,480 and 1,852,800 DOFs, respectively. Fig. 16 shows the approximation of the incompressibility constraint at the cross section $z = 1$ cm at the inflating pressure of 150 mmHg. No strong mesh refining effects are noticeable on the numerical solution suggesting that the approximation of the condition $J = 1$ is mainly affected by the choice of the penalty parameter κ.

The numerical validation of the isotropic and anisotropic constitutive models for the mechanical characterization of healthy cerebral arterial tissue has highlighted both modeling and numerical aspects that should be considered when simulating the arterial wall mechanics. From the modeling point of view, the least squares approximation and the numerical results suggest that, according to the range of transmural pressures of interest, a suitably calibrated isotropic model (as e.g. EXP1 or EXP2) can lead, in terms of the data fitting quality, to equivalent results than an anisotropic one, i.e. the

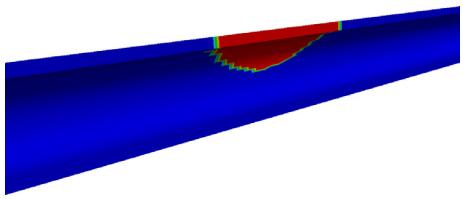

Fig. 17. Representation of the weakened portion of the computational domain.

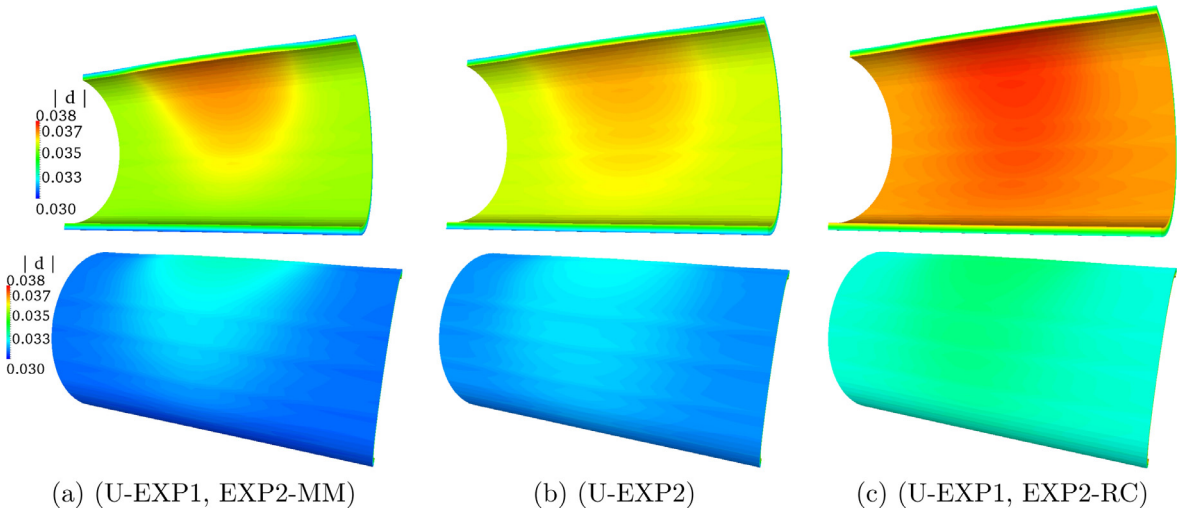

Fig. 18. Case 1: displacement field [cm] at the internal and external surfaces of the computational domain at $\Delta P_{ref} = 110$ mmHg.

(EXP1, EXP2-RC) model. In addition, the possibility of modeling the recruitment of the collagen fibers at finite strains (EXP1, EXP2-MM) instead of at zero strains leads to either a better approximation of the experimental measurements with a good agreement of the numerical results. Moreover, the numerical results obtained using the EXP1, EXP2, (EXP1, EXP2-RC) and (EXP1, EXP2-MM) indicate that when experimental observations of the characteristic directions of collagen fibers are not available on human specimen of arteries, an isotropic model can be a viable alternative to a anisotropic model; this has the advantage of reducing the number of material parameters that need to be estimated and the computational cost of the assembling of the tangent matrix of the first Piola–Kirchhoff tensor.

4.2. Inflation tests on unhealthy cerebral tissue

We now address the numerical simulation of unhealthy cerebral arteries by using the isotropic U-EXP2 and the anisotropic (U-EXP1, EXP2-RC) and (U-EXP1, EXP2-MM) laws. Among the isotropic models, the choice of U-EXP2 is motivated by the good data fitting and agreement between the curve $\mathcal{T}(\lambda_r)$ and the numerical results showed in Fig. 9(c).

We assumed that the weakening of the material properties occurs in a limited portion of the domain, also referred as weakened region, that has been obtained from the intersection of the computational domain with a sphere of radius $r_s = 0.095$ cm and center $C = (0, 0.09, 1.0)$, as indicated in Fig. 17.

Figs. 18 and 19 show the displacement field on the deformed mesh for $\Delta P_{ref} = 110$ mmHg for Case 1 and Case 2 (Section 2.5). In Figs. 18 and 19 the mesh has been deformed according to the displacement field at the reference transmural pressure. We first note that, for each of the two cases under consideration, the maximum value of the displacement magnitude is similar for all the constitutive models. This proves the correct calibration of the weakening parameter D both for Case 1 and Case 2. We also observe that, in both cases the pattern of the displacement fields is affected by the choice of the arterial wall model. The extension and shape of the area where the displacement field is influenced by the weakened region varies with the constitutive model and the weakening parameter D. We observe that in Case 2, where the weakening parameter D for the U-EXP2 and (U-EXP1, EXP2-RC) models is higher than in Case 1, the extension of the area where the displacement field is influenced by the weakened region becomes larger than in Case 1. In particular, for the (U-EXP1, EXP2-RC) model, it reaches the lower part of the cylinder and the displacement field is higher that the one reported for the U-EXP2 model. The displacement field reported in Figs. 18 and 19 indicate the formation of a bulge corresponding to the weakened region of the domain.

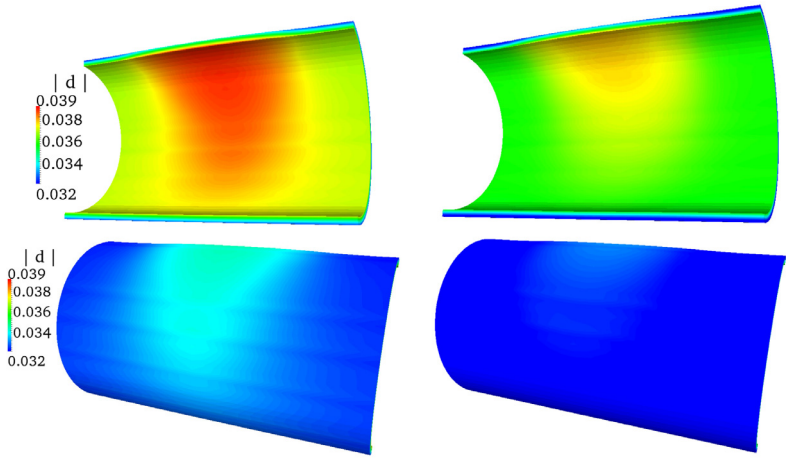

Fig. 19. Case 2: displacement field [cm] at the internal and external surfaces of the computational domain at $\Delta P_{ref} = 110$ mmHg.

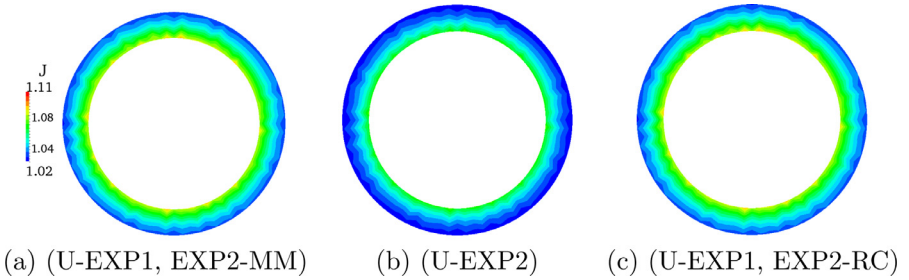

Fig. 20. Case 1: volume ratio J at $\Delta P = 110$ mmHg.

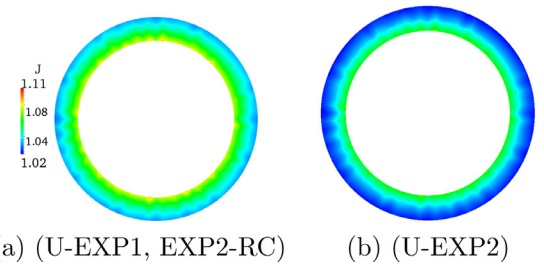

Fig. 21. Case 2: volume ratio J at $\Delta P = 110$ mmHg.

Figs. 20 and 21 report the volume ratio J at $z = 1$ at the reference transmural pressure for Case 1 and 2. As already reported in Fig. 14, the approach used in this work to describe the nearly-incompressible behavior of arteries leads to an acceptable approximation of the incompressibility constraint.

Figs. 22–and 24 show the spatial distribution of the Von Mises stress σ_{VM}(Holzapfel, 2000) in a central portion of the computational domain for Case 1 and Case 2. In this work, residual stresses related to the opening angle of the arterial wall have not been considered, as done e.g. in Dalong et al. (2012); Li and Robertson (2009). Indeed, to the best of our knowledge, experimental observations of the opening angle of cerebral arteries are not available. In addition, residual stresses are not considered here since the analysis presented in Williamson et al. (2003) highlights the fact that the spatial distribution of the mechanical stresses inside the vessel wall is affected principally by the choice of the constitutive model rather than by the introduction of residual stresses. The Von Mises stress σ_{VM} is presented in Fig. 22 only for Case 1 since similar spatial distributions of σ_{VM} have been obtained in both cases under consideration. We remark that in Fig. 22, the Von Mises stress for the three models under consideration has been rescaled in order to show the main qualitative aspects of its spatial distribution. For Case 1, σ_{VM} varies between 3.5×10^5 and 1.5×10^6 dyn/cm^2 and, as expected, the largest value occurs at the internal surface of the cylinder, where the radial displacement is higher. We observe that for Case 1 the Von Mises stress on the internal and external surfaces of the cylinder does not present a strong variability with respect to the constitutive

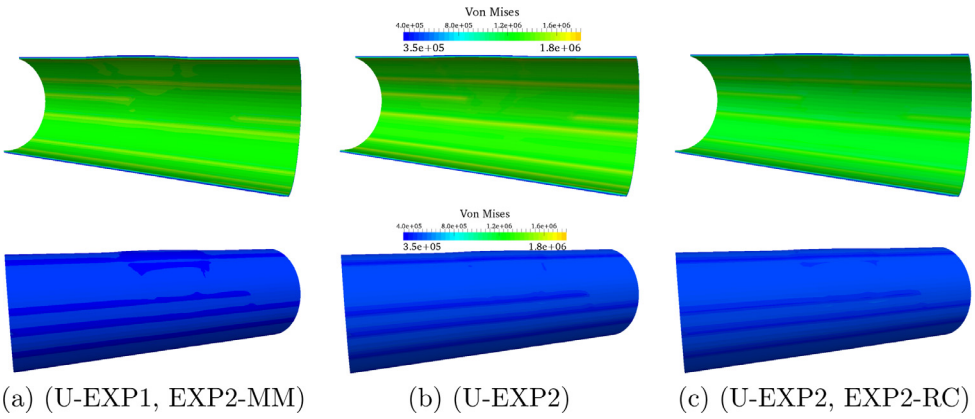

Fig. 22. Case 1: Von Mises stress field [dyn/cm^2] at the internal and external surfaces of the computational domain at $\Delta P_{ref} = 110$ mmHg. The deformation of the vessel wall has been amplified of a factor 1.5 for graphical purposes

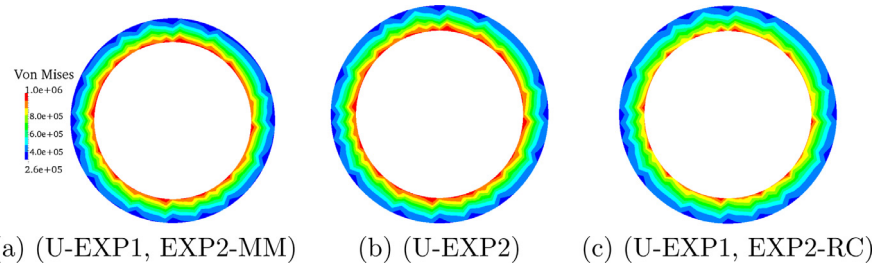

Fig. 23. Case 1: Von Mises stress [dyn/cm^2] on the undeformed cross section at $z = 1$ cm and $\Delta P = 110$ mmHg.

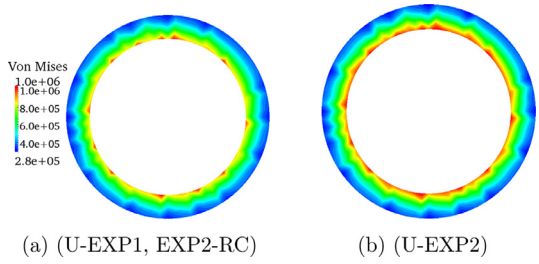

Fig. 24. Case 2: Von Mises stress [dyn/cm^2] on the undeformed cross section at $z = 1$ cm and $\Delta P = 110$ mmHg.

model. This is related to the fact that the displacement field on the internal and external surfaces in Case 1 does not present a strong variability with respect to the constitutive model (as presented in Fig. 18), due to the calibration procedure described in Section 2.5. However, we highlight a significant dependency of the distribution of the Von Mises stress through the thickness of the vessel wall on the constitutive model, as presented in Figs. 23 and 24. In Case 2, the Von Mises stress presents a strong dependency on the constitutive model. More specifically, the different displacement fields in Fig. 19 result in the different pattern of the Von Mises stress. Fig. 24 indicates that for high levels of mechanical weakening, the variations of the Von Mises stress through the thickness of the vessel wall are strongly affected by the choice of the constitutive model. To conclude, Figs. 23 and 24 highlight the relevance of carefully choosing the constitutive model to represent the unhealthy arterial tissue.

4.3. Numerical simulation on a physiological geometry of cerebral artery

We now present and discuss some numerical results obtained on a physiological geometry of a cerebral aneurysm reconstructed from MRI images. Although our results have been obtained from a fluid–structure interaction numerical simulation, we only present the results concerning the mechanical part observed during one heart beat to highlight the influence of the mathematical model for the vessel wall on the numerical results. In this section, for the sake of brevity, we do not address the mathematical formulation of a fluid–structure interaction (FSI) problem, neither we detail the set of initial and boundary conditions considered in this case; in this respect, we refer the interested reader to

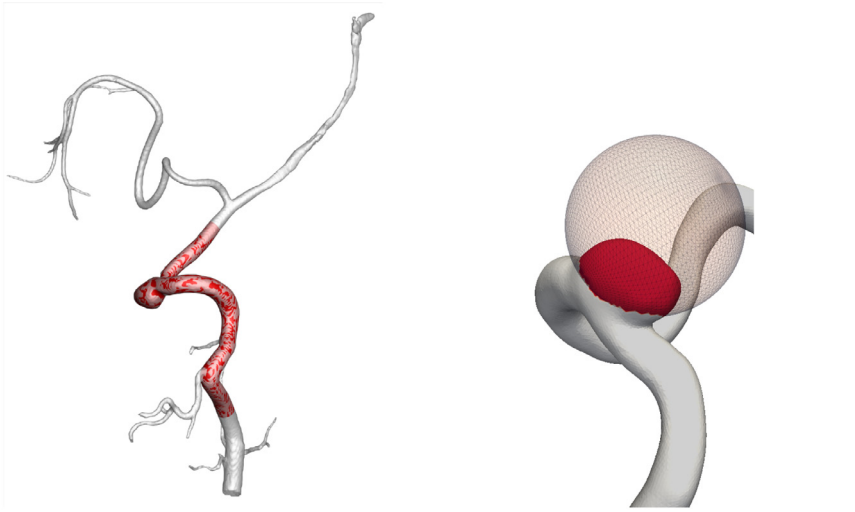

(a) Reconstructed vasculature from MRI images (the portion of interest is colored in red)

(b) Region of mechanical weakening in the aneurysm dome

Fig. 25. Representation of the vascular network in the neck and of the portion of interest.

Table 4
Parameters for the U-EXP1 and U-EXP2 models used for the healthy arterial tissue, weakening parameter D, and parameters for the weakened tissue.

Constitutive model	Material parameters for healthy tissue	Weakening parameter D	Material parameters for weakened tissue
U-EXP2	$\alpha_2 = 5.811\times10^6,\ \gamma_2 = 4.080$	0.25	$\alpha_2 = 4.410\times10^6,\ \gamma_2 = 4.080$
U-EXP1	$\alpha_1 = 4.470\times10^5,\ \gamma_1 = 8.35$	0.15	$\alpha_1 = 3.799\times10^5,\ \gamma_1 = 8.350$

Formaggia, Quarteroni, and Veneziani (2009) and more specifically to Tricerri (2014) and references therein for the detailed description of the mathematical formulation, numerical approximation, initial and boundary conditions for the FSI problem.

The geometry of the patient-specific cerebral aneurysm under consideration is presented in Fig. 25(a). The vascular network reconstructed from the acquired MRI images and the diameter of the parent vessel suggest that the aneurysm in Fig. 25(a) has occurred on the vertebral artery (Gambaruto & João, 2012; Nichols & O'Rourke, 1998; Tricerri, 2014). The blood is modeled as a Newtonian fluid with density ρ_f and dynamic viscosity μ_f equal to $\rho_f = 1.0$ g/cm^3 and $\mu_f = 0.035$ g/(cm s), respectively, while the density of the arterial wall is $\rho_s = 1.2$ g/cm^3. The fluid velocity and pressure are discretized by means of $\mathbb{P}1$Bubble-$\mathbb{P}1$finite elements while linear elements are employed to describe the vessel wall displacement in the structural dynamics problem, as for the static inflation tests. The vessel lumen, i.e. the fluid domain, is composed of 1,013,977 tetrahedral elements while the vessel wall, i.e. the solid domain, is composed of 452,196 tetrahedra. The portion of the solid domain that is considered as mechanically weakened by imposing the constant weakening parameter D reported in Table 4, with respect to the parent vessel which is instead mechanically intact, is detailed in Fig. 25(b). It can be observed that the weakened region in the solid domain corresponds only to the aneurysm dome to take into account the lower mechanical strength of the aneurysmal tissue located at the fundus with respect to the tissue composing the neck of the aneurysm (Humphrey & Canham, 2000).

In our simulations, the vessel wall is modeled by two isotropic models, namely the first (U-EXP1) and second (U-EXP2) order exponential ones in Eqs. (12) and (13). The choice of these two isotropic models is motivated by the facts that no experimental observations on the spatial distribution and orientation of the collagen fibers for the anisotropic models of Section 2.2.4 are available for the geometry under consideration and that, among the isotropic constitutive models described in Section 2.2.3, two exponential laws are able to capture the stiffening effect with increasing stress in arteries as reported in Fig. 3. The material parameters for the U-EXP1 and U-EXP2 isotropic models for the healthy parent vessel and aneurysm walls are provided in Table 4.

The material parameters for the U-EXP1 law describing healthy arterial tissue have been taken from Delfino et al. (1997) for the carotid artery, whose diameter is similar to the one of vertebral arteries (Nichols & O'Rourke, 1998). We assume that the constitutive stress–strain relation characterizing the mechanical response of the healthy tissue has the same form $\mathcal{T} = \mathcal{T}(\lambda_r)$ as in Eq. (26) for a vessel of undeformed internal radius of $r_0 = 0.2$ cm. Prior to setting the weakening parameters

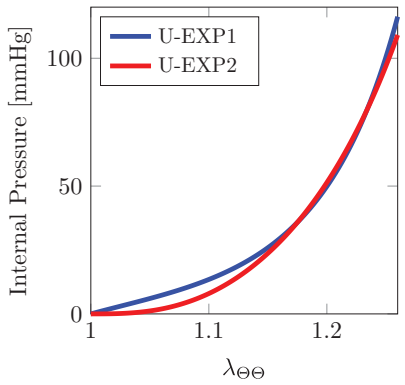

Fig. 26. Stress–strain relations for the U-EXP1 and U-EXP2 models.

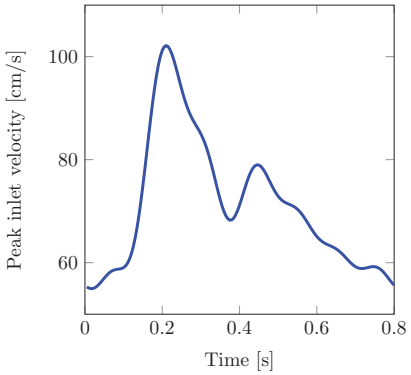

Fig. 27. Peak velocity of the inlet parabolic profile imposed on the inlet boundary of the fluid domain; taken from Baek et al. (2010)

for the two isotropic models under consideration, the second order exponential EXP2 law for the healthy tissue must be adequately calibrated. In this work, the material parameters for the healthy tissue described by the EXP2 law have been determined such that the stress–strain relations $\mathcal{T}_{U-EXP1}(\lambda_r)$ and $\mathcal{T}_{U-EXP2}(\lambda_r)$ intersect at the values of internal pressures of 40 and 100 mmHg. Afterward, we determine the weakening parameters $D_{EXP1} = 0.15$ and $D_{EXP2} = 0.25$ following the same approach described in Section 2.5 and the corresponding presents the stress–strain relations are presented in Fig. 26; we observe that the two curves predict a very similar mechanical response on the range of internal pressures of interest, i.e. $p \in [60, 110]$ mmHg, that is the physiological one.

Arteries deform under the action of the hemodynamical loads due to the blood flow. In order to model a physiological blood flow inside the vessel lumen, at the inlet surface of the fluid domain, a parabolic velocity profile centered with respect to its center is imposed along the inward directed normal unit vector. The time evolution (represented in Fig. 27) of the peak velocity of the parabolic profile is computed from a physiological blood flow profile measured on an Internal Carotid Artery (ICA) (Baek, Jayaraman, Richardson, & Karniadakis, 2010). More in detail, this physiological blood flow has been rescaled with respect to the cross section area of the geometry under consideration.

It is worth pointing out that the velocity values of the inlet profile reported in Fig. 27 are consistent with the experimental measurements available in literature for the cerebral vasculature (Hart & Haluszkiewicz, 2000; Matsuo et al., 2011; Ogoh et al., 2005).

The vessel wall displacement of the entire solid domain at the time $t = 0.2$ s is shown in Fig. 28. The arterial wall displacement is presented only for the U-EXP2 law since the same qualitative behavior for both constitutive laws was observed. The vessel wall displacement in the aneurysm dome is higher with respect to the one measured for the parent vessel due to the combined effect of the mechanical weakening. Moreover, the wall displacement in the parent vessel is directed mainly along the local radial direction, namely the direction perpendicular to the center line of the vessel (Faggiano, Formaggia, & Antiga, 2013). Fig. 28(c) shows the vessel wall displacement at one point of the internal surface of the considered cross section with respect to the undeformed radius. We observe that a variation of 2.5% of the undeformed radius is reported during the heart beat; this result is consistent with the experimental measurements of the variation of the diameter for cerebral arteries presented in Giller, Bowman, Dyer, Mootz, and Krippner (1993); Golemati et al. (2003) for the vertebral and internal carotid artery. Indeed, in Giller et al. (1993) a variation of less than 4% of the arterial radius is reported for the vertebral artery while a minimum variation of 6% is measured in Golemati et al. (2003) for the carotid artery, whose internal radius is similar to the one of the vessel under consideration. By comparing the results presented in Fig. 28(c), we

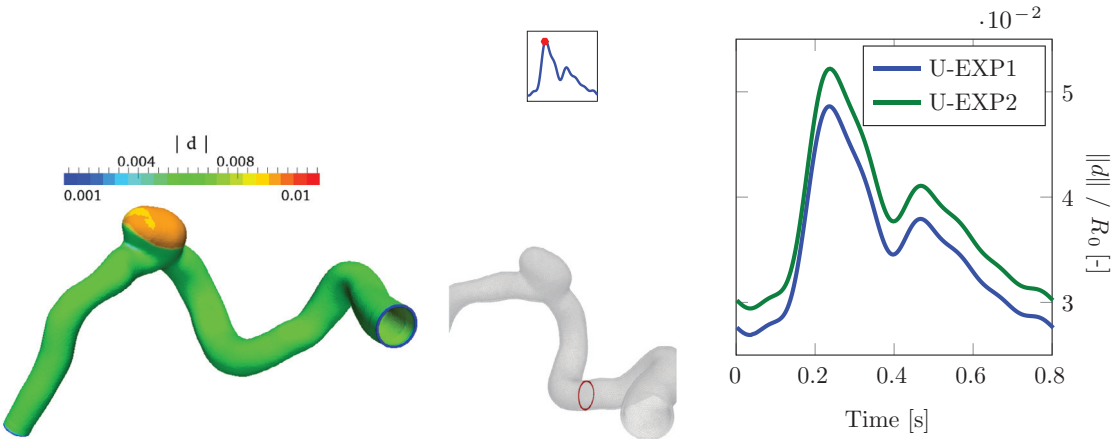

(a) Displacement at time t= 0.2 s for the model U-EXP2 (b) Cross section (c) Relative radial displacement with respect to the undeformed radius R_0

Fig. 28. Vessel wall displacement: (a) snapshot at time $t = 0.2$ s; (b) location of the cross section for the evaluation of the relative vessel wall displacement; (c) relative parent vessel displacement on the internal surface with respect to the internal radius R_0. Blood flow is right to left.

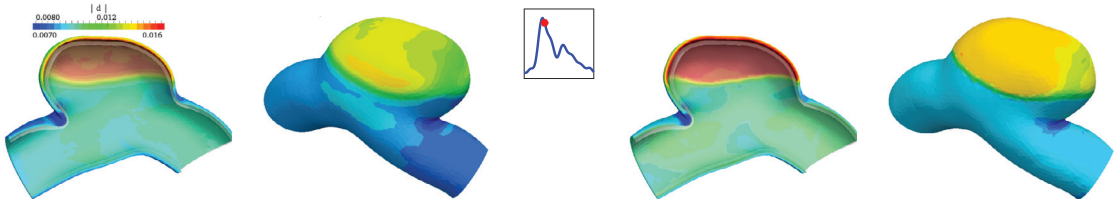

Fig. 29. Vessel wall displacement in the aneurysm dome at the time $t = 0.239$ s. The gray overlay represents the undeformed geometry. The deformations are magnified by a factor 3.

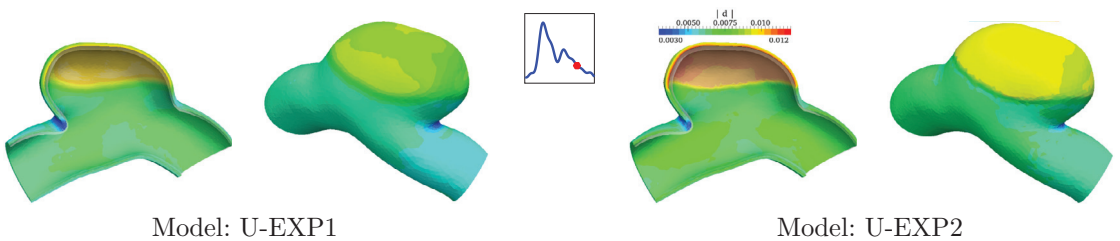

Fig. 30. Vessel wall displacement in the aneurysm dome at the time $t = 0.6$ s. The gray overlay represents the undeformed geometry. The deformations are magnified by a factor 3.

note that the deformations predicted by the two constitutive models are similar during the heart beat; indeed, the maximum displacement at the time $t = 0.239$ s predicted by the U-EXP2 law is 6% higher than the one measured for the U-EXP1 model at the same time.

Figs. 29 and 30 show the displacement of the aneurysm dome during the systole and the diastole. As previously mentioned, it can be observed that the displacement in the parent vessel is mainly directed along the radial direction and that the maximum values are attained in the aneurysm dome where the mechanical weakening occurs. Despite the small quantitative differences among the numerical results, we remark the different qualitative behavior of the two numerical solutions. Indeed, for the entire heart beat, the U-EXP2 model predicts higher displacements than the ones measured with the U-EXP1 law in the whole aneurysm dome. This is of particular interest when considering the influence of the deformations on the progressive mechanical weakening of the arterial tissue and on the development of cerebral aneurysms, as done in Robertson, Hill, and Dalong (2011).

When studying cerebral aneurysms and the factors that may lead to rupture, an important indicator that is evaluated is the dome pulsatility in order to measure the variations of the aneurysm size during the heart beat (Oubel et al., 2010). The

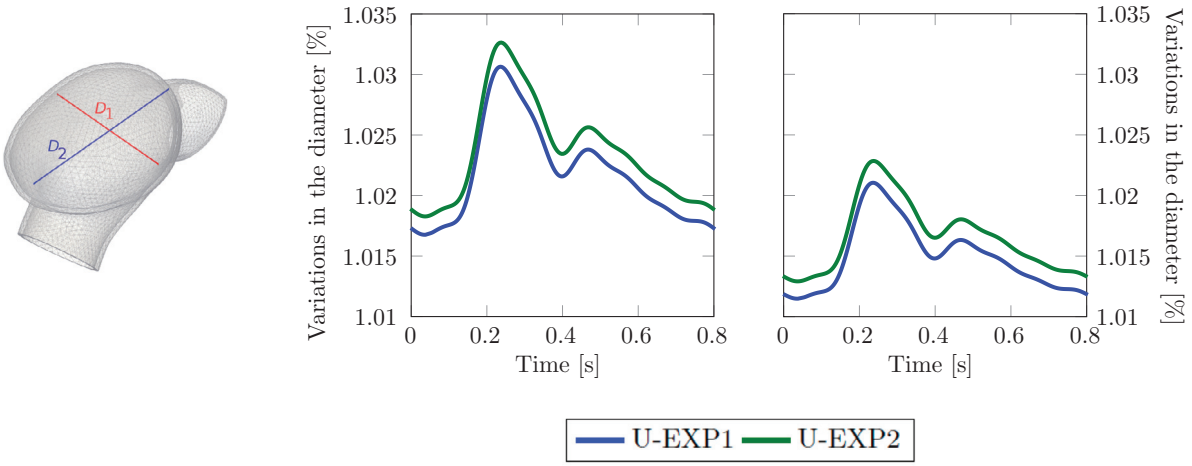

(a) Diameters D_1 and D_2 (b) relative variations in D_1 (c) relative variations in D_2

Fig. 31. Changes in aneurysmal dome diameters; (a) Diameter definition; (b) Relative variations of D_1 with respect to the undeformed diameter D_1 (red line); (c) Relative variations of D_2 with respect to the undeformed diameter D_2 (blue line).

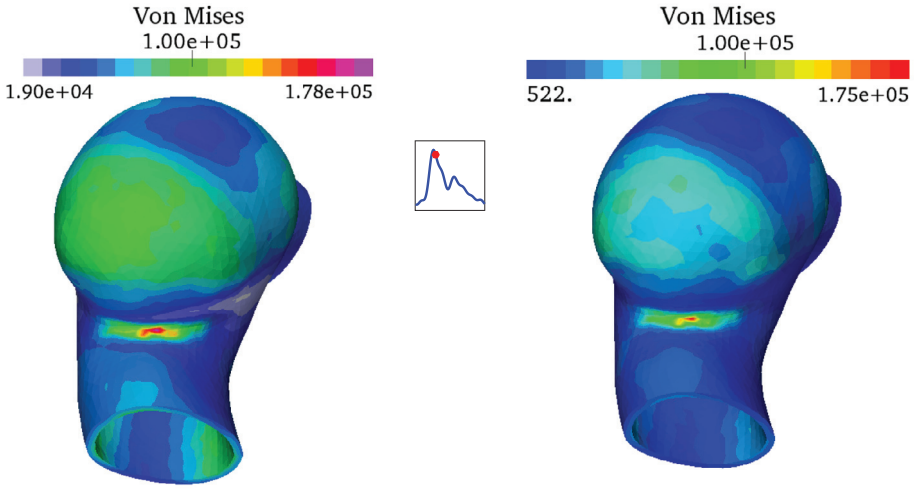

(a) Model: U-EXP1 (b) Model: U-EXP2

Fig. 32. Von Mises stress in the aneurysm dome at the time $t = 0.239$ s.

pulsatility index is a dimensionless quantity defined in Oubel et al. (2010) as

$$\mu = \frac{|\max\{\hat{D_1}, \hat{D_2}\} - \hat{A}|}{D_0}, \tag{37}$$

where $\hat{D_1}$ and $\hat{D_2}$ are the peak-to-peak amplitude of the variations of two characteristic diameters of the aneurysm (D_1 and D_2 in Fig. 31(a)), $\hat{A}$ is the amplitude of variation of the parent vessel diameter during the heart beat, and D_0 is the artery diameter. In this work, D_1 and D_2 have been chosen in order to capture the highest dome displacements along the transverse and parallel directions to the blood flow, while $D_0 = 0.41$ cm close to the dome. The index μ measures the difference in pulsation between the aneurysm and the artery and expresses it as a fraction of the artery diameter. As pointed out in Oubel et al. (2010), the normalization with respect to the artery diameter was added to compare aneurysms at different locations, since the same absolute difference in pulsation changes for arteries of different size. Fig. 31(b) and (c) shows the variations of the two diameters depicted in Fig. 31(a) during the heart beat. We remark that, as previously commented for Figs. 29 and 30, the highest dilatation occurs for the diameter that is oriented transversely with respect to the direction of the blood flow in the parent vessel. We remark that the pulsatility index μ is around 3.3%, which is consistent with the measurements reported in Oubel et al. (2010) for unruptured aneurysms.

Fig. 32 presents the Von Mises stress inside the aneurysm dome at the time corresponding to the largest displacement. We observe that, although the maximum value of Von Mises stress is very similar in both cases, for the U-EXP1 model the region of high stresses is larger than the one obtained with the U-EXP2 law. In particular, the two color scales highlight the different values obtained. As reported in Fig. 32, high values of Von Mises stresses are measured at the downstream apex of the aneurysm dome where, as discussed in Tricerri (2014), the blood flow impinges the vessel wall, while it decreases inside the dome. The analysis of the Von Mises stress inside the aneurysm dome in Fig. 32, indicates the relevance of considering both indicators when describing the progression of the mechanical degradation of the properties of the arterial tissue that occurs in cerebral aneurysms. Indeed, the high and low Von Mises stress regions in the dome can be explained by considering the deformations of the dome during the cardiac cycle, represented in Fig. 29. We conclude that the larger the deformations, the higher the Von Mises stress.

5. Conclusions

In this paper we have presented and discussed different hyperelastic constitutive models, both for isotropic and anisotropic bodies within the context of continua, in particular for cerebral arterial tissue. An in-depth description of the cerebral vasculature and associated diseases is presented, detailing the problem setup and highlighting the sophistication required to accurately simulate such complex problems. The results of the simulations are critically compared to experimental data available in the literature, showing good agreement. While the results and discussion in this work are related to the cardiovascular system, the study is naturally relevant and applicable to a wide set of problems. In particular, our approach for setting the parameters that characterize the constitutive mechanical models, can be used as well in other contexts for modeling complex materials with a limited (and at times contradicting) set of experimental data.

In choosing coefficients and parameters, we find that the isotropic exponential type laws and the models for anisotropic bodies adequately fit the experimental data. The numerical results showed good agreement with the data fitting; moreover, they highlighted the fact that isotropic models can be considered appropriate for arterial tissue when experimental observations of the directions of the collagen fibers in the tissue are not available. Subsequently, the influence of the modeling choice for the unhealthy cerebral arterial tissue on the results of numerical simulations of static inflation tests and fluid–structure interaction simulation on the physiological geometry of a cerebral aneurysm were analyzed. Different levels of mechanical weakening were considered for the vessel wall, employing a dimensionless weakening parameter D both for the static inflation tests and to model the mechanical weakening of the arterial tissue occurring in cerebral aneurysms.

All our numerical simulations have shown that the choice of the type of constitutive model (i.e. isotropic or anisotropic) plays a key role in the spatial distribution of the mechanical stresses through the thickness of the vessel wall. This highlights the relevance of properly selecting the constitutive model when addressing the study of unhealthy conditions of the arterial tissues. However, further numerical validation is necessary to address more complex mechanical tests than the one considered in the present work, and possibly in vivo measurements of the stress–strain relation of arteries. Concerning the anisotropic multi-mechanism model, specifically proposed for cerebral arteries, we have shown that it leads to the best approximation of the experimental measurements.

Acknowledgments

P. Tricerri, A. Gambaruto, and A. Sequeira acknowledge the financial support of Fundação para a Ciência e a Tecnologia (Portugal) through the Research Center CEMAT-IST and the project EXCL/MAT-NAN/0114/2012. P. Tricerri acknowledges the support of the Swiss National Supercomputing Centre (CSCS) under the project ID s391. The authors acknowledge Dr. S. Deparis (EPFL), Professor A.M. Robertson (University of Pittsburgh), and Professor K.R. Rajagopal (Texas A&M University) for the fruitful discussions, help, and advice.

References

Baek, H., Jayaraman, M., Richardson, P., & Karniadakis, G. (2010). Flow instability and wall shear stress variation in intracranial aneurysms. *Journal of the Royal Society Interface, 7*, 967–988.

Baek, S., Rajagopal, K., & Humphrey, J. (2006). A theoretical model of enlarging intracranial fusiform aneurysms. *Journal of Biomechanical Engineering, 128*, 142–149.

Ball, J. (1977). Convexity conditions and existence theorems in nonlinear elasticity. *Archive for Rational Mechanics and Analysis, 63*, 337–403.

Balzani, D. (2006). *Polyconvex anisotropic energies and modeling of damage applied to arterial walls* (Ph.D. thesis). University of Duisburg-Essen.

Balzani, D., Brinkhues, S., & Holzapfel, G. (2012). Constitutive framework for the modeling of damage in collagenous soft tissues with application to arterial walls. *Computer Methods in Applied Mechanics and Engineering, 1*, 139–151.

Balzani, D., Neff, P., Schröder, J., & Holzapfel, G. (2006). A polyconvex framework for soft biological tissues. adjustment to experimental data.. *International Journal of Solids and Structures, 43*, 6052–6070.

Balzani, D., Schöder, J., & Gross, D. (2006). Simulation of discontinuous damage incorporating residual stresses in circumferentially overstretched atherosclerosis arteries. *Acta Biomaterialia, 21*, 609–618.

Bazilevs, Y., Hsu, M., Zhang, Y., Wang, W., Liang, X., Kvamsdal, T., … Isaksen, J. (2010). A fully-coupled fluid–structure interaction simulation of cerebral aneurysms. *Computational Mechanics, 46*, 3–16.

Bell, E., Kunjir, R., & Monson, K. (2013). Biaxial and failure properties of passive rat middle cerebral arteries. *Journal of Biomechanics, 46*, 91–96.

Boyce, M., & Arruda, E. (2000). Constitutive models of rubber elasticity: A review. *Rubber Chemistry and Technology, 73*, 504–523.

Brands, D., Klawonn, A., Rheinbach, O., & Schröder, J. (2008). Modelling and convergence in arterial wall simulations using a FETI solution strategy. *Computer Methods in Biomechanics and Biomedical Engineering, 11*, 569–583.

Brinkhues, S., Klawonn, A., Rheinbach, O., & Schröder, J. (2013). Augmented Lagrange methods for quasi-incompressible material—Applications to soft biological tissue. *International Journal for Numerical Methods in Biomedical Engineering, 29*, 332–350.
Brown, A. (2001). A step-by-step guide to nonlinear regression analysis of experimental data using microsoft Excel spreadsheet. *Computer Methods and Programs in Biomedicine, 65*, 191–200.
Burton, A. (1954). Relation of structure to function of the tissue of the wall of blood vessels. *Physiological Reviews, 34*, 619–642.
Calvo, B., Pêna, E., Martinez, M., & Doblaré, M. (2007). An uncoupled directional damage model for fibred biological soft tissues. formulation and computational aspects. *International Journal for Numerical Methods in Engineering, 69*, 2036–2057.
Carew, T., Vaishnav, R., & Patel, D. (1968). Compressibility of the arterial wall. *Circulation Research, 23*, 61–68.
Chen, J., Wang, S., Ding, G., Yang, X., & Li, H. (2009). The effect of aneurismal-wall mechanical properties on patient-specific hemodynamic simulations: two clinical reports. *Acta Mechanica Sinica, 25*, 677–688.
Ciarletta, P., Izzo, I., Micera, S., & Tendick, F. (2011). Stiffening by fiber reinforcement in soft materials: A hyperelastic theory at large strains and its application. *Journal of the Mechanical Behaviour of Biomedical Materials, 4*, 1359–1368.
Criscione, J., Humphrey, J., Douglas, A., & Hunter, W. (2000). An invariant basis for natural strain which yields orthogonal stress response terms in isotropic hyperelasticity. *Journal of the Mechanics and Physics of Solids, 48*, 2445–2465.
Criscione, J., & Rajagopal, K. (2013). On the modeling of the non-linear response of soft elastic bodies. *International Journal of Non-Linear Mechanics, 56*, 20–24.
Crosetto, P. (2011). *Fluid–structure interaction problems in hemodynamics: Parallel solvers, preconditioners, and applications* (Ph.D. thesis). École Polytechinque Fédérale de Lausanne.
Dalong, L. (2009). *Structural multi-mechanism model with anisotropic damage for cerebral arterial tissues and its finite element modeling*. University of Pittsburgh (Ph.D. thesis)..
Dalong, L., & Robertson, A. (2009). A structural multi-mechanism constitutive equation for cerebral arterial tissue. *International Journal of Solids & Structures, 46*, 2920–2928.
Dalong, L., Robertson, A., Lin, G., & Lovell, M. (2012). Finite element modeling of cerebral angioplasty using a structural multi-mechanism anisotropic damage model. *International Journal for Numerical Methods in Engineering, 92*, 457–474.
Delfino, A., Stergiopulos, N., Moore, J., & Meister, J. (1997). Residual strain effects on the stress field in a thick wall finite element model of the human carotid bifurcation. *Journal of Biomechanics, 30*, 777–786.
Faggiano, E., Formaggia, L., & Antiga, L. (2013). An open-source tool for patient-specific fluid–structure vessel mesh generation. *V International Symposium on Modelling of Physiological Flows (MPF), 2013*, 25–26.
Famaey, N., Sommer, G., Stolen, J., & Holzapfel, G. (2012). Arterial clamping: Finite element simulation and in vivo validation. *Journal of the Mechanical Behavior of Biomedical Materials, 12*, 107–118.
Flory, P. (1961). Thermodynamical relations for high elastic materials. *Transactions of the Faraday Society, 78*, 5222–5235.
Formaggia, L., Quarteroni, A., & Veneziani, A. E. (2009). Cardiovascular mathematics. Modeling and simulation of the circulatory system. *Vol. 1 of MS & A*. Berlin, Heidelberg: Springer-Verlag.
Fung, Y. (1993). *Biomechanics. Mechanical properties of living tissues*. New York: Springer.
Fung, Y., Fronek, K., & Patitucci, P. (1979). Pseudo elasticity of arteries and the choice of its mechanical expression. *American Journal of Physiology, 237*, 1340–1349.
Gambaruto, A., & João, A. (2012). Flow structures in cerebral aneurysms. *Computer & Fluids, 65*, 56–65.
Gasser, T., & Holzapfel, G. (2006). Hyperelastic modelling of arterial layers with distributed collagen fiber orientations. *Journal of the Royal Society, 3*, 15–35.
Gasser, T., Schulze-Bauer, C., & Holzapfel, G. (2002). A three-dimensional finite element model for arterial clamping. *Journal of Biomechanical Engineering, 124*, 355–363.
Giller, C., Bowman, G., Dyer, H., Mootz, L., & Krippner, W. (1993). Cerebral arterial diameters during changes in blood pressure and carbon dioxide during craniotomy. *Neurosurgery, 32*, 737–741.
Golemati, S., Sassano, A., Lever, M., Bharath, A., Dhanjil, S., & Nicolaides, A. (2003). Carotid artery wall motion estimated from B-mode ultrasound using region tracking and block matching. *Ultrasound in Medicine and Biology, 29*, 387–399.
Hart, R., & Haluszkiewicz, E. (2000). Blood flow velocity using transcranial Doppler velocimetry in the middle and anterior cerebral arteries: correlation with sample volume depth. *Ultrasound in Medicine and Biology, 26*, 1267–1274.
Hill, M., Duan, X., Gibson, G., Watkins, S., & Robertson, A. (2012). A theoretical and non-destructive experimental approach for direct inclusion of measured collagen orientation and recruitment into mechanical models of the arterial wall. *Journal of Biomechanics, 45*, 762–771.
Hollander, Y., Durban, D., Lu, X., Kassab, G., & Lanir, Y. (2011). Constitutive modeling of coronary arterial media—Comparison of three model classes. *Journal of Biomechanical Engineering, 133*, 1–35.
Holzapfel, G. (2000). *Nonlinear solid mechanics: A continuum approach for engineering*. England: John Wiley & Sons Ltd.
Holzapfel, G., & Gasser, T. (2000). A new constitutive framework for arterial wall mechanics and a comparative study of material models. *Journal of Elasticity, 61*, 1–48.
Holzapfel, G., & Gasser, T. (2001). A viscoelastic model for fiber-reinforced composites at finite strains: Continuum basis, computational aspects, and applications. *Computer Methods in Applied Mechanics and Engineering, 190*, 4379–4403.
Holzapfel, G., & Ogden, R. (2008). On planar biaxial tests for anisotropic nonlinearly elastic solids. A continuum mechanical framework. *Mathematics and Mechanics of Solids, 14*, 474–489.
Hughes, T. (2000). *The finite element method: Linear static and dynamic finite element analysis*. New York: Dover Publications.
Humphrey, J. (2002). *Cardiovascular solid mechanics. Cells, tissues, and organs*. New York: Springer-Verlag.
Humphrey, J. (2003). Continuum mechanics of soft biological tissues. *The Royal Society, 459*, 3–46.
Humphrey, J., & Canham, P. (2000). Structure, mechanical properties, and mechanics of intracranial saccular aneurysms. *Journal of Elasticity, 61*, 49–81.
Humphrey, J., & Rajagopal, K. (2002). A constrained mixture model for growth and remodeling of soft tissues. *Mathematical Models and Methods in Applied Sciences, 12*, 407–430.
Isaksen, J., Bazilevs, Y., Kvamsdal, T., Zhang, Y., Kaspersen, J., Waterloo, K., … Ingebrigtsen, T. (2008). Determination of wall tension in cerebral artery aneurysms by numerical simulation.. *Stroke, 39*, 3172–3178.
Kachanov, L. (1958). Time of rupture process under creep conditions. *Izvestija Akademii Nauk Sojuza Sovetskich Socialisticeskich Respubliki (SSSR) Otdelenie Techniceskich Nauk (Moskra), 8*, 26–31.
Kamenskiy, A., Dzenis, Y., MacTaggart, J., Lynch, T., Kazmi, S., & Pipinos, I. (2012). Nonlinear mechanics behavior of the human common, external, and internal carotid arteries in vivo. *Journal of Surgical Research, 176*, 329–336.
Kenneth, L., Barbaro, N., & Manley, G. (2008). Biaxial response of passive human cerebral arteries. *Annals of Biomedical Engineering, 36*, 2028–2041.
Kroon, M., & Holzapfel, G. (2008). Estimation of the distributions of anisotropic, elastic properties and wall stresses of saccular aneurysms by inverse analysis. *Proceedings of the Royal Society A, 464*, 807–825.
Li, D., & Robertson, A. (2009). A structural multi-mechanism damage model for cerebral arterial tissue. *Journal of Biomechanical Engineering, 131*, 1–8.
LifeV (2010). École Polytechnique Fédérale de Lausanne (CMCS), CH; Politecnico di Milano (MOX), ITA; INRIA (REO, ESTIME), FR, and Emory University (Math&CS), GA US. LifeV user manual, http://lifev.org.
Malossi, A. (2012). *Partitioned solution of geometrical multiscale problems for the cardiovascular system: Models, algorithms, and applications* (Ph.D. thesis). École Polytechinque Fédérale de Lausanne.
Marquardt, D. (1963). An algorithm for least-squares estimation of nonlinear parameters. *SIAM—Journal on Applied Mathematics, 2*, 431–441.

Matsuo, T., Watanabe, S., Sorimachi, M., Kanda, M., Ohta, Y., & Takahashi, T. (2011). Blood flow velocity waveforms in the middle cerebral artery at rest and during exercise. *Artificial Life and Robotics, 16*, 398–402.
McGloughlin, T. (2011). Biomechanics and mechanobiology of aneurysms. *Studies in mechanobiology, tissue engineering and biomaterials*: vol. 7. Heidelberg: Springer-Verlag.
Miehe, C. (1994). Aspects of the formulation and finite element implementation of large strain isotropic elasticity. *International Journal of Numerical Methods in Engineering, 37*, 1981–2004.
Monson, K. (2001). *Mechanical and failure properties of human cerebral blood vessels* (Ph.D. thesis). University of California, USA.
Monson, K., Barbaro, N., & Manley, G. (2008). Biaxial response of passive human cerebral arteries. *Annals of Biomedical Engineering, 36*, 2028–2041.
Monson, K., Goldsmith, W., Barbaro, N., & Manley, G. (2006). Multiaxial response of human cerebral arteries. *Journal of Biomechanics, 13*, 175–179.
Naghdi, P. (1984). The theory of shells and plates. In *Handbuch der Physick. mechanics of solids: vol. 2*. Berlin, Heidelberg, New York: Springer.
Naghdi, P., & Tang, P. (1977). Large deformation possible in every isotropic elastic membrane. *Philosophical Transactions of the Royal Society A, 287*, 145–187.
Nichols, W., & O'Rourke, M. (1998). *McDonald's blood flow in arteries: Theoretical, experimental, and clinical principles*. London: Arnold.
Nobile, F., Pozzoli, M., & Vergara, C. (2013). Time accurate partitioned algorithms for the solution of fluid–structure interaction problems in haemodynamics. *Computers & Fluids, 86*, 470–492.
Odgen, R. (1997). *Nonlinear elastic deformations*. New York: Courier Dover Publications.
Odgen, R., Saccomandi, G., & Sgura, I. (2004). Fitting hyperelastic models to experimental data. *Computational Mechanics, 34*, 484–502.
Ogoh, S., Fadel, P., Zhag, R., Selmer, C., Jans, I., Secher, N., & Raven, P. (2005). Middle cerebral artery flow velocity and pulse pressure during dynamic exercise in humans. *Heart and Circulation Physiology—American Journal of Physiology, 288*, 1526–1531.
Oubel, E., Cebral, J., De Craene, M., Blanc, R., Blasco, J., Macho, J., … Frangi, A. (2010). Wall motion estimation in intracranial aneurysms. *Physiological Measurements, 31*, 1119–1135.
Polzer, S., Gasser, T., Bursa, J., Staffa, R., Vlachovsky, R., Man, V., & Skacel, P. (2013). Importance of material model in wall stress prediction in abdominal aortic aneurysms. *Medical Engineering & Physics, 35*, 1282–1289.
Quarteroni, A., Sacco, R., & Saleri, F. (2007). *Numerical mathematics*. Berlin, Heidelberg: Springer.
Quarteroni, A., & Valli, A. (1999). *Domain decomposition methods for partial differential equations*. Oxford: Oxford University Press.
Quarteroni, A., & Valli, A. (1999). *Numerical approximation of partial differential equations*. Berlin, Heidelberg: Springer-Verlag.
Quinodoz, S. (2012). *Numerical simulations of orbitally shaken reactors* (Ph.D. thesis). École Polytechinque Fédérale de Lausanne.
Rajagopal, K. (2003). On implicit constitutive theories. *Applications of Mathematics, 48*, 279–319.
Rajagopal, K., & Tao, L. (1995). Mechanics of mixtures. *Advances in mathematics for applied sciences*: vol. 35. Singapore: World Scientific.
Raoult, A. (1986). Non-polyconvexity of the stored energy function of a Saint Venant–Kirchhoff material. *Applications of Mathematics, 31*, 417–419.
Raoult, A. (2009). Symmetry groups in nonlinear elasticity: an exercise in vintage mathematics. *Communications on Pure and Applied Analysis, 8*, 435–456.
Roach, M., & Burton, A. (1957). The reason for the shape of the distensibility curves of arteries.. *Canadian Journal of Biochemistry, 35*, 681–690.
Robertson, A., Hill, M., & Dalong, L. (2011). Structurally motivated damage models for arterial walls. Theory and application. *Modeling of Physiological Flows, MS & A, Springer, 1*, 143–187.
Saad, Y. (1986). *Iterative methods for sparse linear systems*: vol. 7 (2nd ed.).
Scott, S., Ferguson, G., & Roach, M. (1972). Comparison of the elastic properties of human intracranial arteries and aneurysms. *Canadian Journal of Physiology and Pharmacology, 50*, 328–332.
Simo, J., & Taylor, R. (1991). Quasi-incompressible finite elasticity in principal stretches. continuum basis and numerical algorithms. *Computer Methods in Applied Mechanics and Engineering, 85*, 273–310.
Skrzypek, J., & Ganczarski, A. (1999). *Modeling of material damage and failure of structures*. Berlin, Heidelberg: Springer-Verlag.
Sommer, G., Regitnig, P., Költringer, L., & Holzapfel, G. (2010). Biaxial mechanical properties of intact and layer-dissected human carotid arteries at physiological and supraphysiological loadings. *American Journal of Physiology. Heart and Circulatory Physiology, 298*, 898–912.
Spencer, A. (1971). *Theory of invariants*. Academic Press.
Spencer, A. (1984). *Continuum theory of the mechanics of fibre-reinforced composites, CISM courses and lectures*. Wien: Springer-Verlag.
Torii, R., Oshima, M., Kobayashi, T., Takagi, K., & Tezduyar, T. (2006). Fluid–structure interaction modeling of aneurysmal conditions with high and normal blood pressures. *Computational Mechanics, 43*, 151–159.
Torii, R., Oshima, M., Kobayashi, T., Takagi, K., & Tezduyar, T. (2008). Fluidâ–structure interaction modeling of a patient-specific cerebral aneurysm: Influence of structural modeling. *Computational Mechanics, 38*, 482–490.
Tricerri, P. (2014). *Mathematical and numerical modeling of healthy and unhealthy cerebral arterial tissues* (Ph.D. thesis). Instituto Superior Técnico and École Polytechinque Fédérale de Lausanne.
Tricerri, P., Dedè, L., Deparis, S., Quarteroni, A., Robertson, A., & Sequeira, A. (2015). Fluid–structure interaction simulations of cerebral arteries modeled by isotropic and anisotropic constitutive laws.. *Computational Mechanics, 55*, 478–498.
Truesdell, C., & Noll, W. (1965). *The nonlinear field theories of mechanics*. Berlin, Heidelberg, New York: Springer-Verlag.
Valencia, A., Burdiles, P., Ignat, M., Mura, J., Bravo, E., Rivera, R., & Sordo, J. (2013). Fluid structural analysis of human cerebral aneurysm using their own wall mechanical properties.. *Computational and Mathematical Methods in Medicine, 2013*, 1–18.
Weisbecker, H., Pierce, D., & Holzapfel, G. (2011). Modeling of damage-induced softening for arterial tissue. In *Proceedings of the 2011 SCATH joint workshop on new technologies for computer/robot assisted surgery* (pp. 1–4).Graz, Austria.
Williamson, S., Lam, Y., Younis, H., Huang, H., Patel, S., Kaazempur-Mofrad, M., & Kamm, R. (2003). On the sensitivity of wall stresses in diseased arteries to variable material properties. *Journal of Biomechanical Engineering, 125*, 147–155.
Wulandana, R., & Robertson, A. (2005). An inelastic multi-mechanism constitutive equation for cerebral arterial tissue. *Biomechanics and Modeling in Mechanobiology, 4*, 235–248.